

DISSERTATION

**GCM simulation
of Earth-like planets
for photometric lightcurve analysis**

(地球型惑星のGCMシミュレーションと
それを用いた光度曲線解析)

中川 雄太

A thesis submitted to
the graduate school of science,
the University of Tokyo
in partial fulfillment of
the requirements for the degree
of
Master of Science in Physics

January, 2018

Abstract

Since the first discovery of an exoplanet, many astronomical measurements have revealed various physical parameters of exoplanets. These parameters include those of sizes, orbital motions, and surface environments such as atmospheres or clouds of exoplanets. It is natural that we next aim to detect more detailed parameters - spin motion and surface distribution of exoplanets.

The scattered light curve analysis of direct imaged exoplanets is expected to be a powerful method to detect the spin motion and surface distribution of exoplanets. Nevertheless the angular resolution of the planet have been lost, they could recover these information by using the diurnal and annual periodicities of light curves. The spin and orbital motion gradually changes the apparent image of the exoplanet as if they scan the planetary surface. Because its measurement needs much more developed instruments than they achieved, these previous studies have used observational data of the Earth (as a habitable exoplanet) or simulated light curves assuming some simple situation (cloudless Earth, static cloud Earth).

A previous study constructed a model estimating the spin motion (planetary obliquity and spin frequency) of an exoplanet from the frequency modulation of the light curve and introduced the analytic method of simulated light curves. The noteworthy point of this is that they focused on the frequency domain, which is complementary to the method on other studies which have focused amplitude variability of light curves often contaminated by statistical noises. In their simulation, they assumed that the planet is an Earth having a static albedo distribution, in other words the effect of clouds is omitted.

The effects of clouds on the planetary light curve is significantly important because the reflectance of clouds is larger than those of lands or ocean. More to say, clouds are not static contrary to the assumption, covering the planetary surface to disturb the periodic variability of light curves. This is our motivation of this thesis that we validate the estimation method on cloudy Earth using the frequency modulation.

In this thesis, we calculate the dynamical motion of clouds on Earth with different planetary obliquity, simulate the planetary light curves, and estimate the planetary spin parameters including the obliquity and spin frequency. We use some public codes in every steps.

First, we calculate the dynamical motion of clouds. To express it consistently, we use a GCM (Global Climate Model) and calculate the atmospheric structure of Earths with various planetary obliquity, 0° , 15° , 30° , 45° , 60° , 75° , and 90° . The other planetary parameters we used are those of the Earth.

Second, we simulate the planetary light curves with a radiative transfer model for the Earth atmosphere. We calculate the scattered intensity of each surface pixel and integrate them. These light curves are about three times brighter than those of

cloudless Earths. The periodicities of them are definitely modulated by the motion of clouds.

Finally, we estimate the spin parameters from its light curve using the frequency modulation method. We only perform the estimation for the no or little oblique cases 0° and 15° , and we estimated the spin parameters well in spite of the effect of clouds. It indicates that the clouds trace the planetary surface enough to produce the original photometric variabilities. In highly oblique cases, we must check our results in all steps.

Contents

1	Introduction	1
2	A review on previous studies	4
2.1	Direct imaging of exoplanets	4
2.1.1	Concept of Direct Imaging	4
2.1.2	Time resolved imaging of exoplanets	7
2.2	Frequency modulation on the planetary light curve due to the planetary obliquity	11
2.2.1	Maximum weighted longitude approximation of the apparent rotational frequency modulation	13
2.2.2	Time-frequency analysis for extracting the instantaneous frequency	17
2.3	Structure and Dynamics of planetary atmosphere	19
2.4	General Circulation Model	22
3	General Circulation Model	25
3.1	Setup and Sub-grid physical processes	27
3.2	Initial Condition	28
3.3	Climates of Earth twins with various obliquities	30
4	Mock observation of planets	41
4.1	Geometric configuration	41
4.2	Model assumption in the radiative transfer calculation	42
4.2.1	Planetary surface: lands	42
4.2.2	Planetary surface: ocean	42
4.2.3	Atmosphere and clouds	43
4.2.4	Setup	45
4.3	Light curves and images of Earth twins	48
5	Time-frequency analysis of light curves	52
5.1	Setup of the time-frequency representation	52
5.2	Band dependence on the time-frequency representation	52
5.3	Effects of noises on the time-frequency representation	53
5.4	Obliquity dependence on the time-frequency representation	57

5.5 Estimation of the planetary obliquity	61
6 Summary and Future prospects	66
Acknowledgments	67

Chapter 1

Introduction

From the first discovery of an extrasolar planet (exoplanet) by Mayor & Queloz (1995), the exoplanet science has developed dramatically. Especially in recent years, the scientific stage gradually shifts from “the detection age” to “the characterization age”, which allows us to know a lot of information about exoplanets (mass, radius, orbital parameters, atmosphere, surface, spin parameters, ... life?).

Mayor & Queloz (1995) detect an exoplanet by the radial velocity method using the sinusoidal change of the spectrum of the host star due to the gravitational interaction with its planet. This method provides the information of the planetary mass and some orbital parameters. The transit method detecting the periodic dip of the photometric stellar light curve due to the planetary occultation (e.g., Henry et al. 2000) provides the information of the planetary radius and some orbital parameters. Berta et al. (2012) performed the spectrum observation during a planetary transit and confirmed the atmospheric composition of a planet from the difference of the transit depth (the transmission spectra method). Direct imaging method is a promising method to characterize some planetary parameters (e.g., Kuzuhara et al. 2013; Marois et al. 2008).

Future space missions will provide the photometric, direct-imaging, long time monitoring, well time-resolved light curves of terrestrial extrasolar planets. The variability of the planetary scattered light is considered to allow us to characterize the planetary surface and its spin parameters (Ford et al. 2001). The inversion techniques that retrieve the surface distribution from light curves are well studied for future missions (e.g., Cowan et al. 2009, Fujii et al. 2010, Fujii et al. 2011, Kawahara & Fujii 2011, Fujii & Kawahara 2012).

A complementary method to these inversion techniques which enable us to estimate the spin parameters, planetary obliquity and spin frequency, without the retrieval of the surface distribution are proposed by Kawahara (2016). He focused on the frequency domain of the photometric variability, not the amplitude modulation which is used in the surface distribution inversion. He used the fact that the apparent diurnal periodicity of light curve is modulated by the orbital and spin motion. He constructed a model of the frequency modulation induced by the planetary obliquity and compared it with the simulated photometric frequency of a cloudless static Earth. The model

agreed well with the simulation and well retrieved not only the obliquity but also the spin frequency.

In this thesis, we attempt to apply the obliquity estimation method of Kawahara (2016) to the Earth with time varying clouds and investigate the capability of the estimation under the effect of clouds. In fact, almost half of the Earth's surface is covered by clouds. High reflectance of clouds significantly affects the scattered light curve. Clouds are not static; move, generate, and disappear. It is not assumed in Kawahara (2016). Cloud pattern of an Earth with a different obliquity should be different from that of the Earth. Figure 1.1 shows the schematic procedure of this study. In order to represent the cloud pattern on another oblique Earth consistently,

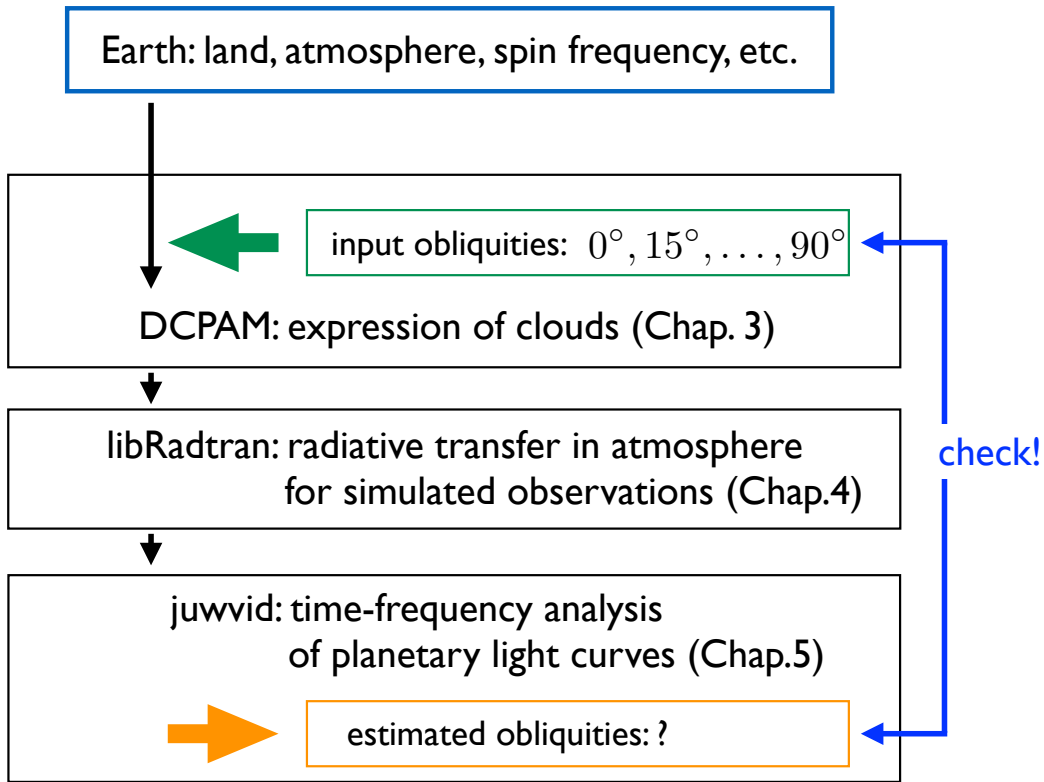


Figure 1.1: R map in the $(\Theta_{\text{offset}}, \zeta)$ plane.

we calculate the three-dimensional atmospheric circulation and cloud formation with GCM (Global Climate Model or General Circulation Model). The GCM we use in this thesis is DCPAM5 (Takahashi et al. 2016) which is utilized for planets with various parameters. We employ the parameter set of the Earth except for the obliquity. The values of obliquity we employ are 0° , 15° , 30° , 45° , 60° , 75° , and 90° . Using their planetary parameters, we obtain scattered photometric light curves from a radiative transfer calculation and its time-frequency representation from the pseudo-Wigner distribution. In the case of the frequency modulation on low oblique planets, we

compare it with the model described in Kawahara (2016). We find the spin parameters which reproduce the input ones well. Since the frequency modulation of highly oblique planets are difficult to determine, we extend these work to a future study.

In chapter 2, we review photometric variability of direct imaged exoplanets and planetary atmosphere. We also show the mathematical formulation used in following chapter. In chapter 3, we describe the configuration of GCM experiments and briefly show the results. In chapter 4, we describe the configuration of radiative transfer calculation and briefly show the light curves and planetary images. Finally, in chapter 5, we discuss the frequency modulation of cloudy planets in terms of the dynamics of clouds and estimate the obliquity in some cases, supplemented with the future prospect on this study.

Chapter 2

A review on previous studies

2.1 Direct imaging of exoplanets

Direct imaging is an observational method to take a snapshot of the exoplanet system suppressing the bright star's image and diffraction. In this section, we briefly summarize the concept of direct imaging and inversion technique, without the detailed mentions about their instruments. We basically follow Seager (2010).

2.1.1 Concept of Direct Imaging

The two important parameters in direct imaging of exoplanets are the angular separation and star-planet flux contrast of planet. Angular separation is the distance of a planet and a star in celestial sphere. When the distance from observer to star is $d(\text{pc})$ and the semi-major axis of planet is $a(\text{au})$, the maximum angular separation $\theta_{sp}(\text{arcsec})$ is

$$\theta_{sp} \simeq a/d. \quad (2.1)$$

The direct imaging instrument should have an angular resolution, $\Delta\theta$, much smaller than θ_{sp} . The telescope diameter determines the maximum angular resolution from the diffraction limit:

$$\Delta\theta \simeq \lambda/D, \quad (2.2)$$

where the unit of $\Delta\theta$ is radian, where λ is wavelength, D is telescope diameter. If we want to image directly an exoplanet at 1au around a star at 10pc at $0.5\mu\text{m}$, for instance, we need $D \sim 3\text{m}$ telescope diameter at least.

The contrast C is defined to be the ratio of planet-to-star flux toward observer,

$$C(\lambda) = \frac{F_p(\lambda)}{F_s(\lambda)}, \quad (2.3)$$

where $F_p(\lambda)$ depends on the properties of the planetary surface and the apparent geometry of the planetary system. The smaller C makes it easier to image the planet

directly. In general, the spectrum of a planet consists of reflected starlight and thermal emission:

$$F_p(\lambda) = F_p^{ref}(\lambda) + F_p^{emi}(\lambda). \quad (2.4)$$

When we consider the Sun-Earth system which has a significant temperature difference (5800K to 300K), one of the two components dominates depending on the wavelength. From UV to NIR the reflected component F_p^{ref} is dominant having a peak of $\sim 0.5\mu\text{m}$, whereas the thermal component F_p^{emi} is dominant from MIR around a peak of $\sim 10\mu\text{m}$. Typical contrast depends on the wavelength, more to say, on the dominant spectral component.

First we consider the visible brightness of planet. For simplicity, we assume that the reflected starlight follows the Lambert law. The Lambert law states that the light incident on a surface is reflected isotropically in all directions in the sense of intensity. It means that the flux of the reflected light on a surface toward an observer is proportional to the projected area in the reflected direction. Similarly to this, a surface receives the amount of light which is proportional to the projected area in the incident direction. We introduce the albedo $A(\lambda)$, which are defined to be the ratio of total incident flux to total leaving flux. If an element of a surface with the area dS receives light with the flux of $F(\lambda)$ from the incident zenith angle of ϑ_0 and reflects them in the ratio of $A(\lambda)$ with the intensity of $I(\lambda)$, we can write the equation of flux conservation in each wavelength:

$$A(\lambda)F(\lambda) \cos \vartheta_0 dS = \int_{\Omega_1} I(\lambda) dS \cos \vartheta_1 d\Omega_1, \quad (2.5)$$

where Ω_1 is the upper sphere of solid angle, and ϑ_1 is the scattering zenith angle. It can be easily solved as

$$I(\lambda) = \frac{A(\lambda)F(\lambda) \cos \vartheta_0}{\pi}. \quad (2.6)$$

We can also derive the flux from the whole planet to an observer with the phase angle (the angle of star-planet-observer) α ,

$$\begin{aligned} F_p^{ref}(\lambda) &= \int_{S_p} \frac{A(\lambda)F(\lambda) \cos \vartheta_0}{\pi} \cos \vartheta_1 dS_p \frac{1}{d^2} \\ &= \int_{\Omega_p} \frac{A(\lambda)F(\lambda) \cos \vartheta_0}{\pi} \cos \vartheta_1 d\Omega_p \left(\frac{R_p}{d}\right)^2. \end{aligned} \quad (2.7)$$

In the above S_p and Ω_p is the planet surface area and normalized surface that is illuminated and visible, θ_p and ϕ_p are the normalized planet surface coordinate. To solve the phase function, we adopt the orbital coordinate system where the unit vector from the planet to the host star is $\vec{e}_S = (1, 0, 0)^T$, the unit vector from the planet to the observer is $\vec{e}_O = (\cos \alpha, \sin \alpha, 0)^T$, the unit vector from the planetary center to

the surface is $\vec{e}_R = (\sin \theta_p \cos \phi_p, \sin \theta_p \sin \phi_p, \cos \theta_p)^T$, as shown in Figure. 2.1. From these components, we obtain $\cos \vartheta_0 \equiv \vec{e}_S \cdot \vec{e}_R$ and $\cos \vartheta_1 \equiv \vec{e}_O \cdot \vec{e}_R$. Then

$$\begin{aligned} &= \int_0^\pi \sin \theta_p d\theta_p \int_{\alpha-\pi/2}^{\pi/2} d\phi_p \frac{A(\lambda)F(\lambda)}{\pi} \sin \theta_p \cos \phi_p \cdot \sin \theta_p \cos(\phi_p - \alpha) \left(\frac{R_p}{d}\right)^2 \\ &= \frac{2}{3} \phi(\alpha) A(\lambda) F(\lambda) \left(\frac{R_p}{d}\right)^2, \end{aligned} \quad (2.8)$$

and $\phi(\alpha)$ represents the geometric effect on the reflected light, often called as the Lambert phase function. The phase function $\phi(\alpha)$ is normalized to satisfy $\phi(\alpha=0)=1$:

$$\phi(\alpha) = \{(\pi - \alpha) \cos \alpha + \sin \alpha\} / \pi. \quad (2.9)$$

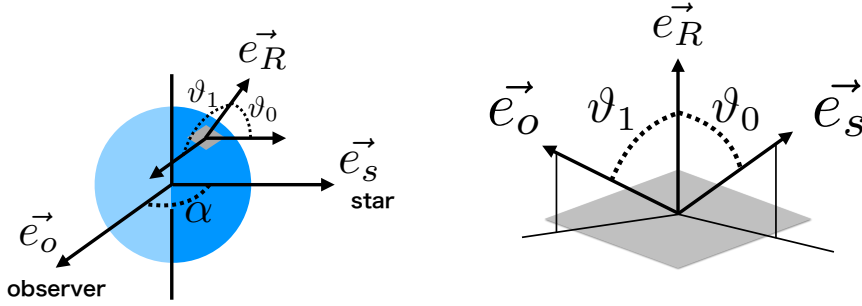


Figure 2.1: Schematic configuration of planetary surface. Now we set the coordinate system based on the position of the star and the observer as shown in the left panel. The right panel shows the zoom-up view of a surface element to describe the projected components $\cos \vartheta_0$ and $\cos \vartheta_1$.

The visible contrast is given by

$$\begin{aligned} C &= \frac{2}{3} \phi(\alpha) A(\lambda) \frac{L_*(\lambda)}{4\pi a^2} \left(\frac{R_p}{d}\right)^2 / \frac{L_*(\lambda)}{4\pi d^2} \\ &= \frac{2}{3} \phi(\alpha) A(\lambda) \left(\frac{R_p}{a}\right)^2. \end{aligned} \quad (2.10)$$

For example, the contrast of the Earth-Sun system with the phase of $\alpha=\pi/2$, the quarter Earth, assuming to be Lambert sphere is

$$C \simeq 10^{-10}, \quad (2.11)$$

where we adopt an average of albedo $A = 0.3$.

Next we consider the infrared brightness of a planet. If a planet is in radiative equilibrium, that is, all the absorbed energy are emitted as thermal radiation, and we can write the equation of bolometric flux conservation as

$$(1 - A_{Bond})\pi R_p^2 \frac{4\pi R_* \sigma T_*^4}{4\pi a^2} = 4\pi f R_p^2 \sigma T_{equil}^4, \quad (2.12)$$

where A_{Bond} is the Bond albedo, which is defined to be the bolometric albedo, σ is the Stefan-Boltzmann constant, f is a efficiency factor of the intra-surface energy distribution, and T_{equil} is the equilibrium temperature. We obtain the equilibrium temperature,

$$T_{equil} = \left(\frac{1 - A_{Bond}}{4f} \right)^{1/4} \left(\frac{R_*}{a} \right)^{1/2} T_*. \quad (2.13)$$

For example, the equilibrium temperature of the Earth is $T_{equil}=255\text{K}$, when we assume the values of $A_{Bond}=0.3$ and $f=1.0$. It represents the temperature of the effective radiative altitude $\sim 40\text{km}$. The actual surface temperature of the Earth is $\sim 290\text{K}$, which is $\sim 30\text{K}$ warmer than T_{equil} due to the greenhouse effect. We estimate the infrared contrast by assuming that planet and star are blackbodies. In this case we have

$$C(\lambda) = \frac{B(\lambda, T_p) R_p^2}{B(\lambda, T_*) R_*^2}, \quad (2.14)$$

where T_p is the planet temperature, $B(\lambda, T)(\text{W m}^{-2} \mu\text{m}^{-1} \text{str}^{-1})$ is the Planck function:

$$B(\lambda, T) = \frac{2hc^2}{\lambda^5} \frac{1}{\exp(hc/\lambda k_B T) - 1}, \quad (2.15)$$

with h being the Planck constant. By substituting Equation (2.15) into Equation (2.14), we can rewrite

$$C(\lambda) = \left(\frac{\exp(hc/\lambda k_B T_*) - 1}{\exp(hc/\lambda k_B T_p) - 1} \right) \left(\frac{R_p}{R_*} \right)^2, \quad (2.16)$$

and we find the contrast of the Earth at wavelength of $\lambda=10\mu\text{m}$:

$$C(\lambda) \simeq 8.4 \times 10^{-8}. \quad (2.17)$$

From Equation (2.16), we can estimate T_p and R_p by multi band photometry of thermal emission even in the case of exoplanets.

2.1.2 Time resolved imaging of exoplanets

In order to naively resolve the image of a planet at 10pc in visible wavelength, we find that we need hundreds of km telescope diameter from Equation (2.2). Instead of

making such an unrealistic equipment, it is suggested to use the time resolved direct imaging method to secondarily resolve the planet image.

The scattered light on a planetary surface depends on the optical properties there, including atmospheres, surfaces, and clouds. If the properties of the planetary surface change in time, not only the dynamical change on the surface but also the apparent change due to the spin motion and the orbital motion, they can also vary the scattered light. When we assume that there is no dynamical change on the planetary surface and the albedo distribution is inhomogeneous, the variability of the scattered light curve should be caused only by the planetary motion and encode the information of the planetary surface. Therefore, we can resolve the planetary image from the variation of planetary light curves.

In this section the discussion and definition of the formula basically follow Fujii & Kawahara (2012). To compute planetary light curves, we define the inertia coordinate system modified from Fujii & Kawahara (2012). First we introduce the spherical coordinate system θ (latitude) and ϕ (longitude) as shown in Figure 2.2. Note that θ is defined as the latitude, contrary to the colatitude employed in Fujii & Kawahara (2012) so as to adapt to the GCM coordinate system. This is the only difference. To describe the spin motion, they defined $\Phi(t)$ to be the angle between the direction of equinox and the origin of ϕ , which changes in time as the planet spins. We obtain the spin phase function by using the spin angular frequency ω_{spin} :

$$\Phi(t) = \omega_{\text{spin}}t + \Phi_{\text{offset}}. \quad (2.18)$$

They also defined $\Theta(t)$, the orbital phase function, to have its origin on the superior conjunction $\Theta = 0$ and increases in time to correspond $\Theta = 2\pi$ after one orbital motion. The direction of the spin axis is denoted by obliquity ζ and orbital phase of vernal equinox Θ_{eq} as shown in Figure 2.3. The obliquity ζ is defined to be the angle between the spin and orbital angular momentum vectors. The orbital phase of vernal equinox Θ_{eq} is the parameter specifying the azimuthal angle of the spin vector, defined to be the angle between the position of the planet at the superior conjunction and at the vernal equinox.

Three unit vectors were introduced to describe the configuration of the planetary system; the vector from planetary center to the host star \vec{e}_S , the vector from planetary center to the observer \vec{e}_O , and the vector from planetary center to the surface \vec{e}_R . For simplicity, we assume the distant-observer distant-star approximation which states that the observer and the star is distant from the planet enough to regard the vector from the surface to the star and observer as parallel to \vec{e}_S and \vec{e}_O , respectively. We can write the components of the three unit vectors as

$$\vec{e}_S = \begin{pmatrix} \cos(\Theta - \Theta_{\text{eq}}) \\ \sin(\Theta - \Theta_{\text{eq}}) \\ 0 \end{pmatrix}, \quad (2.19)$$

$$\vec{e}_O = \begin{pmatrix} \sin i \cos \Theta_{\text{eq}} \\ -\sin i \sin \Theta_{\text{eq}} \\ \cos i \end{pmatrix}, \quad (2.20)$$

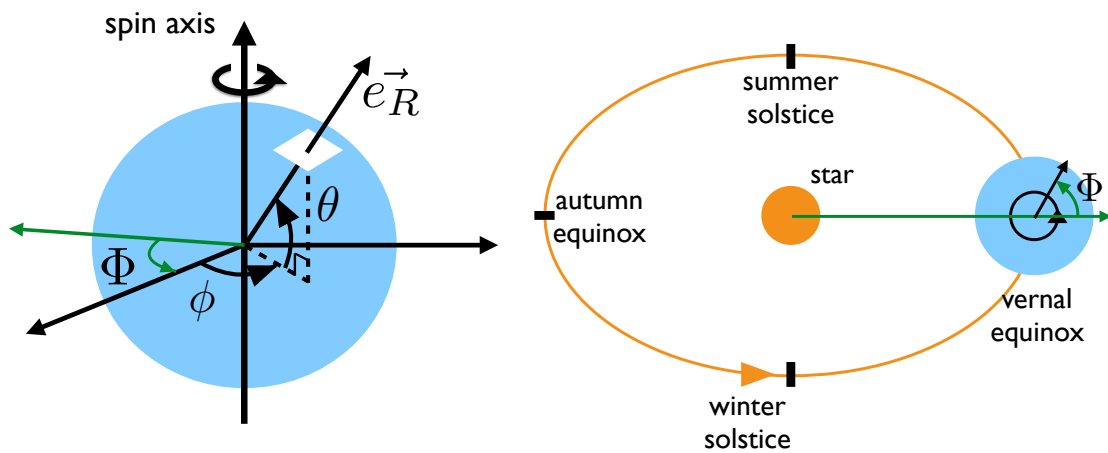


Figure 2.2: Schematic configuration of planetary surface and system reproduced from Fujii et al. (2010). The left panel shows the spherical coordinate, latitude θ and longitude ϕ . The green arrow shows the direction of vernal equinox (also shown in the right panel), which aligns the equatorial plane. The right panel shows the definition of $\Phi(t)$, the spin phase function, as if we view the circular orbit from the direction of planetary spin axis. The black and green arrows on the planet show the direction of the prime meridian and vernal equinox.

$$\vec{e}_R = R_x(\zeta) \vec{e}_R'(\phi + \Phi, \theta) \quad (2.21)$$

$$= \begin{pmatrix} \cos(\phi + \Phi) \cos \theta \\ \sin(\phi + \Phi) \cos \theta \cos \zeta + \sin \theta \sin \zeta \\ -\sin(\phi + \Phi) \cos \theta \sin \zeta + \sin \theta \cos \zeta \end{pmatrix}, \quad (2.22)$$

where $R_x(\zeta)$ is the rotation operator around x -axis to tilt the spin axis and $\vec{e}_R'(\phi, \theta) = (\cos \phi \cos \theta, \sin \phi \cos \theta, \sin \theta)^T$ is the vector specifying a surface element in surface coordinate system.

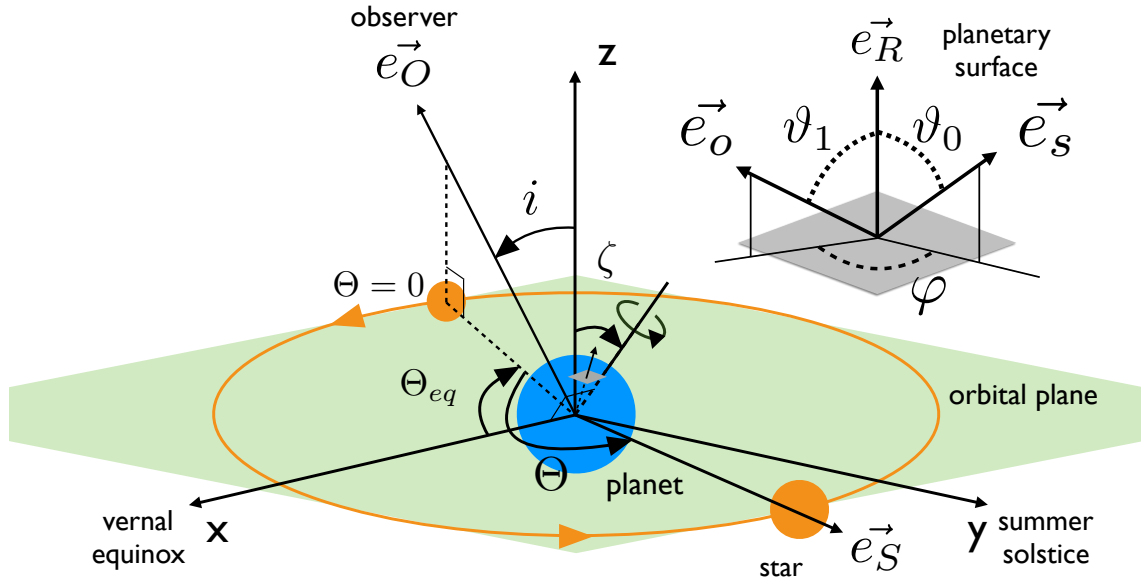


Figure 2.3: Schematic configuration of the system and observer reproduced from Fujii & Kawahara (2012). The direction of the observer \vec{e}_O and the spin vector do not change, while only the direction of the star \vec{e}_S does change in time.

Next we focus on the scattering process on the planetary surface. Bi-directional reflectance distribution function (BRDF) is often used for the approximation of the scattering property of the land surface and the remote sensing of the Earth. BRDF characterizes the intensity distribution of the reflected light and has the dimension of str^{-1} . BRDF is a function of the direction of incident and scattered ray, sometimes omitted the absolute azimuthal angle assuming that there is no proper direction on the surface. In this case, the BRDF is expressed as $f(\vartheta_0, \vartheta_1, \varphi; \lambda)$, where ϑ_0 , ϑ_1 , and φ are the incident zenith angle, scattering zenith angle, and relative azimuthal angle between the incident azimuthal angle and scattering azimuthal angle as shown in 2.3, and wavelength λ . Since the BRDF is defined in terms of intensity, the scattered intensity at planetary surface is written as

$$I(\vartheta_0, \vartheta_1, \varphi; \lambda) = F_*(\lambda) \cos \vartheta_0 f(\vartheta_0, \vartheta_1, \varphi; \lambda), \quad (2.23)$$

where $F_*(\lambda)$ ($\text{W m}^{-2} \mu\text{m}^{-1}$) is the incident stellar flux.

We show an example, the Lambertian (isotropic) scattering model. From Equation (2.6), BRDF of a Lambertian surface is written as

$$f(\vartheta_0, \vartheta_1, \varphi; \lambda) = \frac{A(\theta, \phi; \lambda)}{\pi}, \quad (2.24)$$

where $A(\theta, \phi; \lambda)$ is the albedo at the planetary surface denoted as (θ, ϕ) at wavelength λ . Note that ϑ_0 , ϑ_1 , and φ are functions of geometric parameters \vec{e}_S , \vec{e}_O , and \vec{e}_R . The scattered flux of the whole planet is

$$F(\lambda) = \frac{R_p^2}{\pi d^2} \int_{\Omega} A(\theta, \phi; \lambda) W_I(\theta, \phi) W_V(\theta, \phi) d\Omega, \quad (2.25)$$

where W_I and W_V is the functions of the apparent weight of the illuminated and visible area, defined to be $W_I(\theta, \phi) \equiv \max\{\cos \vartheta_0, 0\}$ and $W_V(\theta, \phi) \equiv \max\{\cos \vartheta_1, 0\}$.

These weight functions are functions of time because the geometric parameters change in time.

2.2 Frequency modulation on the planetary light curve due to the planetary obliquity

Kawahara (2016) suggested to use the frequency modulation on the planetary light curves as a probe of the obliquity. His method focused on only the frequency not amplitude of light curve variation allows to identify the obliquity of a planet even from noisy data. In this section we briefly review its concept, model and analysis.

He first consider a prograde planet (obliquity $\zeta = 0^\circ$) and observer in the direction $i = 0^\circ$ (face-on). He assume that the planet has a static surface distribution. The rotation frequency $f_{\text{spin}} = 1/P_{\text{spin}}$ is the inverse of sidereal day of the planet P_{spin} , the period in which the planet spins once relative to the inertia frame ¹. It does not correspond to the frequency of the light curve variation because the light curve variation should correspond to the frequency of synodic day, which is the period needed for the central star to cross the planetary meridian. This apparent periodicity f_{obs} is given by

$$f_{\text{obs}} = f_{\text{spin}} - f_{\text{orb}}, \quad (2.26)$$

where $f_{\text{orb}} = 1/P_{\text{orb}}$ is the orbital frequency and P_{orb} is the orbital period. For retrograde planets (obliquity $\zeta = 180^\circ$), we obtain the apparent periodicity as

$$f_{\text{obs}} = f_{\text{spin}} + f_{\text{orb}}. \quad (2.27)$$

For a planet with an obliquity between 0° and 180° , how does the apparent periodicity?

We next consider a $\zeta = 90^\circ$ planet as shown in Figure 2.4, for the schematic explanation of the apparent periodicity of generally oblique planets. The left panel

¹We can also say that $f_{\text{spin}} = \omega_{\text{spin}}/2\pi$ by using the above definition.

shows a face-on view of the planetary system. Panel (a) shows a zoom-in picture of the planet. The red solid cross is the representative point of the illuminated and visible area and the dotted cross is the representative point after one spin period. The green line is a meridian of the planet. After one spin motion, the longitude of the representative point becomes larger than before due to the orbital motion, which indicates that it needs more time to show an apparent photometric variation, that is, the apparent frequency is smaller than the spin frequency. Panel (b) shows the planet after one quarter of orbital motion. In this condition, the longitude of representative point does not show a significant change. Therefore the apparent rotational frequency here is almost the same as the spin frequency. In panel (c), the longitudinal shift of the representative point is backward of that in panel (a), decelerating the apparent rotational frequency. Thus, the apparent rotational frequency can modulate in an orbital motion and it is accelerated or decelerated by the longitudinal shift of the representative point of the illuminated and visible area of a planet.

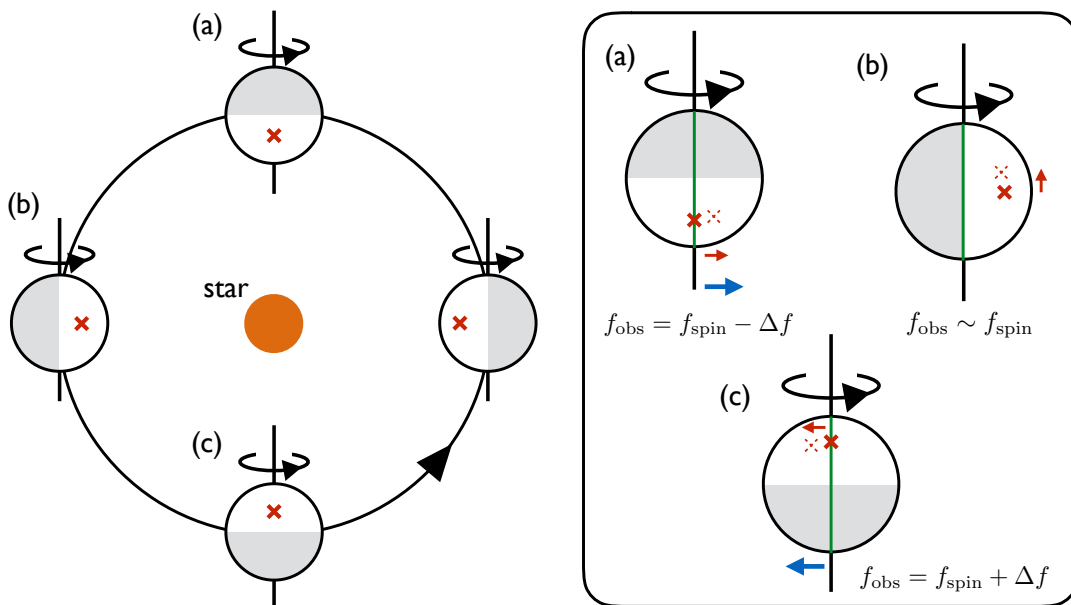


Figure 2.4: The orbital configuration of a $\zeta = 90^\circ$ planet viewed from the direction of $i = 0^\circ$ (face-on), reproduced from Kawahara (2016) in order to describe the concept of geometric frequency modulation. Panel (a) shows a zoom-in picture of planet. The solid and dotted red cross shows the representative point of the illuminated and visible area and that of one rotation period after. The red arrows show the direction of the time variation of the representative point. The green line indicates of a meridian on the planet. The blue arrows indicate the longitudinal variation of the representative point. The longitudinal shift of the representative point accelerate or decelerate the apparent rotational frequency.

The frequency modulation is also seen in different geometries, such as inclined viewing observer. Figure 2.5 shows the case of a transiting planet with $\zeta = 0^\circ$, viewed

from $i = 90^\circ$ (edge-on). We omit some symbolic illustration used in the previous figure but we only show the position of the representative points and their instantaneous longitudinal shifts. In the case of inclined planets ($i \neq 0^\circ$), the phase angle α changes in time:

$$\begin{aligned} \cos \alpha &= \vec{e}_S \cdot \vec{e}_O \\ &= \sin i \cos \Theta. \end{aligned} \quad (2.28)$$

The annual change of the phase angle α can cause not only the amplitude modulation during a year which basically follows the Lambert phase function (Equation 2.9) but also the frequency modulation. In the case of Figure 2.5, the representative point shifts from left to right, delaying the apparent periodicity than the sidereal day.

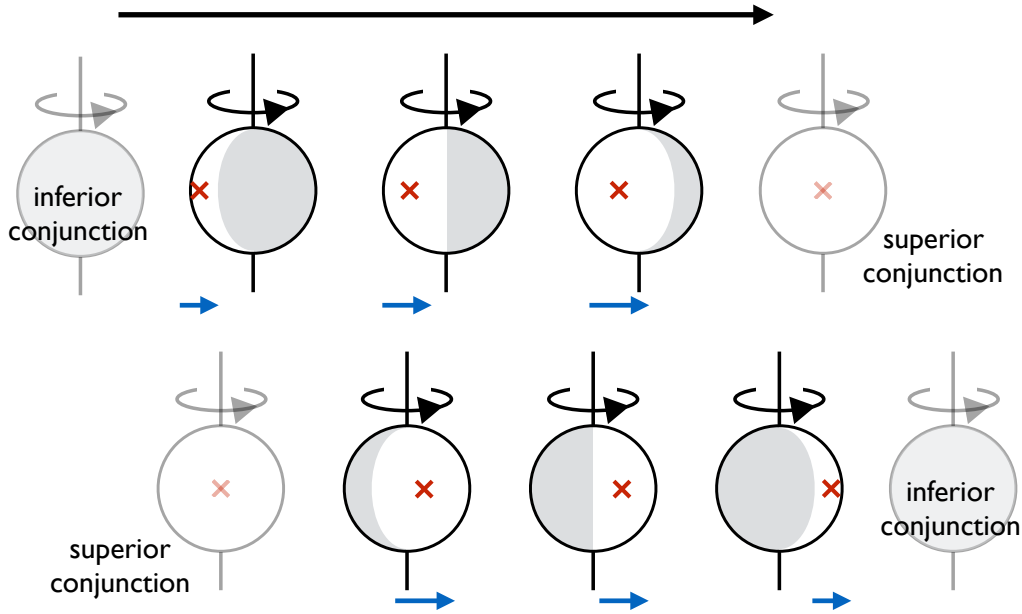


Figure 2.5: Schematic illustration of an inclined planetary system reproduced from Kawahara (2016).

2.2.1 Maximum weighted longitude approximation of the apparent rotational frequency modulation

He gave a simple model of the frequency modulation of the apparent rotational periodicity which is described by the shift of longitude of the representative point of the illuminated and visible area $\hat{\phi}_M$, that he called as the *Maximum weighted longitude approximation*. In fact, the apparent rotational frequency depends on both the rotation and the albedo distribution, as shown in Equation 2.25. However, the key of this approximation is to neglect the effect of the albedo distribution on the apparent rotational frequency, but only to use the inhomogeneity of them generating the variability.

He explained the apparent variability by using the maximum weighted longitude $\hat{\phi}_M$. If the planetary obliquity $\zeta = 0$ and the observer $i = 0$, $\hat{\phi}_M$ changes in the negative direction because the planet rotates eastward. The velocity of the longitudinal shift is a constant $2\pi(f_{\text{spin}} - f_{\text{orb}})$, and we obtain $\hat{\phi}_M = -\Phi + \Theta = -2\pi(f_{\text{spin}} - f_{\text{orb}})t$.

We go back to the nonzero obliquity case. Based on the concept of maximum weighted longitude, he gave the instantaneous frequency as

$$f_{\text{obs}} = -\frac{1}{2\pi} \frac{\partial \hat{\phi}_M}{\partial t} = -\frac{\partial \hat{\phi}_M}{\partial \Theta} f_{\text{orb}}. \quad (2.29)$$

In order to extract the spin component, he used

$$\frac{\partial(\hat{\phi}_M + \Phi)}{\partial \Theta} = \frac{\partial \hat{\phi}_M}{\partial \Theta} + \frac{f_{\text{spin}}}{f_{\text{orb}}}, \quad (2.30)$$

separating the spin and orbital component,

$$f_{\text{obs}} = f_{\text{spin}} + \epsilon_\zeta(\Theta) f_{\text{orb}}, \quad (2.31)$$

where ϵ_ζ is the modulation factor,

$$\epsilon_\zeta(\Theta) \equiv \frac{\partial(\hat{\phi}_M + \Phi)}{\partial \Theta}. \quad (2.32)$$

Let us derive the modulation factor ϵ_ζ . The illuminated and visible weight $W_I \cdot W_V$ takes its maximum at the maximum weighted point in his definition. From the law of reflection, the maximum weighted point corresponds to the point satisfying $\vartheta_0 = \vartheta_1$ and $\varphi = \pi$, and we can write the vector from the planetary center to the maximum weighted point $e_M^{\vec{}}$ as

$$e_M^{\vec{}} = \frac{e_S^{\vec{}} + e_O^{\vec{}}}{|e_S^{\vec{}} + e_O^{\vec{}}|} \quad (2.33)$$

$$= \frac{1}{L} \begin{pmatrix} \cos(\Theta - \Theta_{eq}) + \sin i \cos \Theta_{eq} \\ \sin(\Theta - \Theta_{eq}) - \sin i \sin \Theta_{eq} \\ \cos i \end{pmatrix}, \quad (2.34)$$

where $L = \sqrt{2 + 2 \sin i \cos \Theta}$. To compute the longitude of the maximum weighted point in the spherical coordinate system, he multiply $R_x(-\zeta)$ by $e_M^{\vec{}}$

$$R_x(-\zeta)e_M^{\vec{}} = \frac{1}{L} \begin{pmatrix} \cos(\Theta - \Theta_{eq}) + \sin i \cos \Theta_{eq} \\ \cos \zeta [\sin(\Theta - \Theta_{eq}) - \sin i \sin \Theta_{eq}] - \sin \zeta \cos i \\ \sin \zeta [\sin(\Theta - \Theta_{eq}) - \sin i \sin \Theta_{eq}] + \cos \zeta \cos i \end{pmatrix} \quad (2.35)$$

$$= \begin{pmatrix} \cos(\hat{\phi}_M + \Phi) \cos \hat{\theta}_M \\ \sin(\hat{\phi}_M + \Phi) \cos \hat{\theta}_M \\ \sin \hat{\theta}_M \end{pmatrix}. \quad (2.36)$$

Thus, he obtained

$$\tan(\hat{\phi}_M + \Phi) = \frac{\cos \zeta [\sin(\Theta - \Theta_{eq}) - \sin i \sin \Theta_{eq}] - \sin \zeta \cos i}{\cos(\Theta - \Theta_{eq}) + \sin i \cos \Theta_{eq}}. \quad (2.37)$$

Using the relation

$$\frac{\partial \arctan x}{\partial x} = \frac{1}{1 + x^2}, \quad (2.38)$$

he defined as $\kappa(\Theta) \equiv \tan(\hat{\phi}_M + \Phi)$ and obtained the modulation factor

$$\begin{aligned} \epsilon_\zeta(\Theta) &= \frac{\kappa'(\Theta)}{1 + \kappa^2(\Theta)} \\ &= \frac{\{-\cos \zeta + \sin \zeta \cos i \sin(\Theta - \Theta_{eq}) - \cos \zeta \cos \Theta \sin i\}}{\{\cos^2(\Theta - \Theta_{eq}) \\ &\quad + [-\cos \zeta \sin(\Theta - \Theta_{eq}) + \cos \zeta \sin \Theta_{eq} \sin i + \sin \zeta \cos i]^2 \\ &\quad + 2 \cos \Theta_{eq} \sin i \cos(\Theta - \Theta_{eq}) + \cos^2 \Theta_{eq} \sin^2 i\}}. \end{aligned} \quad (2.39)$$

Upper panels of Figure 2.6 show several examples of the modulation factor of the maximum weighted longitude approximation on different geometry. The horizontal axis shows the orbital phase Θ in radian, the vertical axis shows the planetary obliquity ζ in radian, and the colors show the modulation factor $\epsilon_\zeta(\Theta)$. The singular points of the modulation factor are also shown in the figure by the green points. On the singular point, the maximum weighted point corresponds to the north or south pole $e_M = \pm e_{\text{spin}}$, which does not allow to define the maximum weighted longitude. Lower illustration shows the singular points for the leftmost example $(i, \Theta_{eq}) = (0^\circ, 0^\circ)$. From Equation (2.35), we obtain the values of the singular points $(\tilde{\zeta}, \tilde{\Theta})$:

$$\cos(\tilde{\Theta} - \Theta_{eq}) = -\sin i \cos \Theta_{eq}, \quad (2.40)$$

$$\tan \tilde{\zeta} \cos i = \pm \sqrt{1 - \sin^2 i \cos^2 \Theta_{eq}} - \sin i \sin \Theta_{eq}. \quad (2.41)$$

In general there are two singular points having different values of $\tilde{\zeta}$ for given (i, Θ_{eq}) . The modulation factor shows positive and negative peaks above and below a singular point.

He suggested the classification of the instantaneous frequency curves based on the two singular points; (a) $\zeta \leq \tilde{\zeta}_I$, (b) $\tilde{\zeta}_I < \zeta < \tilde{\zeta}_{II}$, and (c) $\tilde{\zeta}_{II} \leq \zeta$, where $\tilde{\zeta}_I$ and $\tilde{\zeta}_{II}$ ($\tilde{\zeta}_I < \tilde{\zeta}_{II}$) are the obliquity of the singular points. In each domain, the instantaneous frequency curves show a similar modulation pattern as shown in Figure 2.7: $\epsilon_\zeta(\Theta)$ shows one negative modulation, one positive and one negative modulation, and one positive modulation in domain (a), (b), and (c) respectively. The vertical axis shows the modulation factor. The horizontal axis shows the orbital phase, which corresponds to the time. They exhibit the peak proper to the belonging domain.

These domains almost correspond to the three types of spin states, prograde (low oblique), pole-on ($\zeta \sim 90^\circ$), and retrograde (inverted). The modulation patterns are significantly different between three domains although $\zeta = 0^\circ$ and $\zeta = 180^\circ$ are difficult to distinguish because of their featureless modulation.

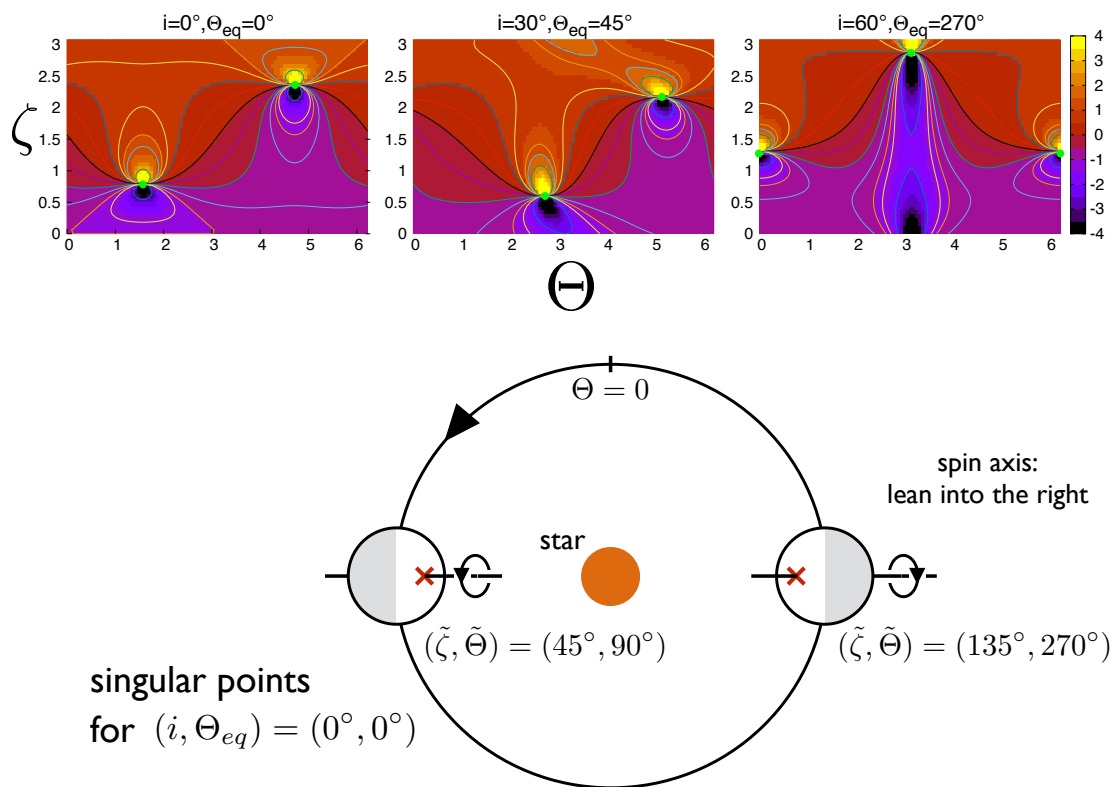


Figure 2.6: Examples of the modulation factor $\epsilon_\zeta(\Theta)$ of the maximum weighted approximation reproduced from Kawahara (2016). As the planet orbits, the modulation factor changes in time from left to right in a figure. He showed three cases $(i, \Theta_{eq}) = (0^\circ, 0^\circ), (30^\circ, 45^\circ), (60^\circ, 270^\circ)$. The lower panel shows two planets corresponding to the singular points.

$$(i, \Theta_{eq}) = (0^\circ, 0^\circ) \rightarrow (\tilde{\zeta}_I, \tilde{\zeta}_{II}) = (45^\circ, 135^\circ)$$

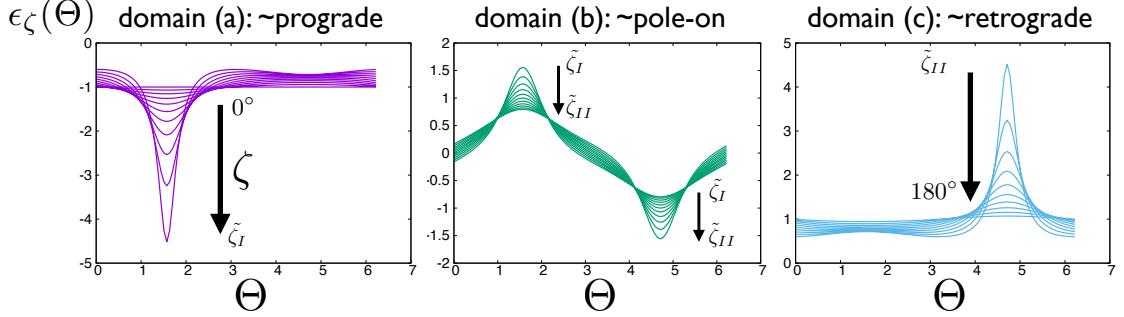


Figure 2.7: Examples of the modulation factor $\epsilon_\zeta(\Theta)$ of the maximum weighted approximation. In this figure, we set $i = 0^\circ$ and $\Theta_{eq} = 0^\circ$, corresponding to $\tilde{\zeta}_I = 45^\circ$ and $\tilde{\zeta}_{II} = 135^\circ$. We show 10 modulation curves in each panel: (a) $\zeta = 0^\circ - 36^\circ$, (b) $\zeta = 72^\circ - 108^\circ$, and (c) $\zeta = 144^\circ - 180^\circ$.

2.2.2 Time-frequency analysis for extracting the instantaneous frequency

He also gave an estimation method of the instantaneous frequency using time-frequency analysis and compare Equation (2.39) with the simulations of the planetary light curve.

He used the static cloud-subtracted Earth proposed by Kawahara & Fujii (2011), whose surface albedo is static and has the land distribution of the Earth. These albedo is determined by the color difference and cloud fraction. In their paper they subtracted the retrieved albedo map between the different colors so as to retrieve the effect of clouds. Contrary to them, he did use the color difference map modified by the cloud fraction as input.

He equally divide one year into 4096 time grids and obtain the photometric flux in each time step from Equation (2.25) to make the photometric light curve. Only for the analytic interest, he added the Gaussian noises with the standard deviation $\sigma_n = 0$ and σ_s to the light curve, where σ_s is the standard deviation of the photometric variation.

In order to estimate the instantaneous frequency of the apparent variation, he adopted the pseudo-Wigner distribution as the time-frequency representation. The time-frequency representation describes the signal in both time and frequency domains in the form of amplitude or energy density. We briefly summarize their extracting method. The pseudo-Wigner distribution is one of the time-frequency representation expressed as

$$g(f, t) = \int_{-\infty}^{\infty} h(\tau) z(t + \tau/2) z^*(t - \tau/2) e^{-2\pi i f \tau} d\tau, \quad (2.42)$$

where z and z^* is the signal and its complex conjugate, and $h(\tau)$ is the window function to reduce the cross terms. He used the Hamming window in the form of sinusoidal

curve

$$h(\tau) = \begin{cases} 0.54 + 0.46 \cos(2\pi\tau/\omega) & \text{for } |\tau| \leq \omega/2 \\ 0 & \text{otherwise,} \end{cases} \quad (2.43)$$

where ω is the window width. The pseudo-Wigner distribution takes the Fourier transform of the windowed autocorrelation of the data, emphasizing the periodicity near the time of interest, and reducing the cross terms and noises.

The discrete form of Equation (2.42) is given by

$$g(f, t_i) = \sum_{|m| \leq M} h[m] z[i+m] z^*[i-m] e^{-2\pi i f \cdot 2m}, \quad (2.44)$$

where $M = \min\{i-1, N-i\}$. Since $g(f, t_i)$ is written in the form of normalized energy density, he extract the instantaneous frequency from the time-frequency representation using the formula

$$\hat{f}(t_i) = \operatorname{argmax}_{[f_m, f_M]} g(f, t_i), \quad (2.45)$$

where f_m and f_M are the minimum and maximum frequency of interest.

He generated the analytic signal $\{z[i]\}$ less dependent on the amplitude modulation by following the steps below. First of all, he divide the data into 64 sets containing 64 data points and compute their mean and standard deviation in each set. By subtracting the mean from the light curve, dividing by the standard deviation, and connecting them in time sequence, he obtained the analytic signal. Since the obtained analytic signal is always real, we can omit the * in Equation 2.44 in this case.

Using these techniques, he analyzed the instantaneous frequency of the mock photometric light curves. In order to compare the model curve and the extracted instantaneous frequency, he use the Levenberg-Marquardt algorithm (mpfit, Markwardt 2009) and fit them excluding the signals of the both ends ~ 19 days. The parameters i and P_{orb} are fixed because they will be constrain the previous observations exposed for a longer time. He fitted with the remaining free parameters ζ , Θ_{eq} , and P_{spin} . The estimated parameters ζ and Θ_{eq} were in good agreements with the input value, although there were slight shifts of a few tens of degrees caused by the albedo distribution. On the other hand the estimated P_{spin} agreed well with the input one, with an accuracy of \sim hours per year.

Finally, as he mentioned, this frequency estimator is good achievement for atmosphereless planets, because the frequency modulation of their photometric light curves is dominated by the geometric effect. In thin-atmosphere planets like Earth, the cloud effect is important because they are dynamic and their large reflectance dominate the photometric variability. Our aim of this thesis is the investigation of the dynamical cloud effect on the planetary light curve and its frequency modulation, and the application of the techniques of Kawahara (2016).

2.3 Structure and Dynamics of planetary atmosphere

We briefly summarize the structure and dynamics of planetary atmosphere. Planet binds gas materials by the gravity and forms the atmosphere. Planet has two characteristic radii for gas retention where another force balances with the gravitational force. The region of planetary atmosphere, if it exists, should be limited within these two radii, and outside of the core radius.

One of the radii is the Hill radius where the stellar tidal force balances with the gravitational force:

$$R_{\text{Hill}} = a \left(\frac{M_p}{3M_*} \right)^{1/3}, \quad (2.46)$$

where M_p is mass of the planet, M_* is mass of the central star, and a is the semi-major axis. The derivation is as follows: for a object to orbit circularly around the star with the same period P at some position on inferior conjunction balancing the star gravity and the planet gravity, the distance from the planet d should obey the equation of statics:

$$0 = -\frac{GM_*}{(a-d)^2} + (a-d) \left(\frac{2\pi}{P} \right)^2 + \frac{GM_p}{d^2}. \quad (2.47)$$

By substituting P in Equation (??), we obtain

$$\left\{ 1 - \left(1 - \frac{d}{a} \right)^3 \right\} \left(\frac{d}{a} \right)^2 = \frac{M_p}{M_*} \left(1 - \frac{d}{a} \right)^2. \quad (2.48)$$

If we assume that $d/a \ll 1$ and neglect the second term of d/a in each side, Equation (2.48) provides

$$3 \left(\frac{d}{a} \right)^3 \simeq \frac{M_p}{M_*} \quad \rightarrow \quad d = a \left(\frac{M_p}{3M_*} \right)^{1/3} \equiv R_{\text{Hill}}. \quad (2.49)$$

In the region within the radius R_{Hill} , objects are stably orbiting around the planet.

The other one is the Bondi radius where the gas thermal motion balances with the planet gravity:

$$R_{\text{Bondi}} \simeq \frac{GM_p}{k_B T / m}, \quad (2.50)$$

where k_B is the Boltzmann constant, T is the gas temperature, and m is molecular mass. In the region outside the radius R_{Bondi} , the thermal velocity of an atom or molecule ($v_{th} = \sqrt{\frac{k_B T}{m}}$) exceeds the escape velocity of the planet ($v_{es} = \sqrt{\frac{GM_p}{R_{\text{Bondi}}}}$), as a result the gas escapes progressively to space (*thermal escape*).

Figure ?? shows the relation between the planet mass M and the above radii R . We assume that the host star is the Sun, the planet has $1au$ orbit, 300K gas temperature,

1.0g/mol gas molecular weight, and 5g/cm^3 mean core mass density. If the planet has the mass larger than the lunar one ($\sim 10^{-2}M_{\oplus}$), the planet can acquire the atmosphere.

Next we consider the one dimensional structure of the spherical symmetric atmosphere. We use five equations to solve them. The first is the equation of hydrodynamic equilibrium

$$\frac{dP}{dr} = -\frac{GM_r}{r^2}\rho, \quad (2.51)$$

where P is the gas pressure, r is the radial coordinate, ρ is the gas density, and M_r satisfies the equation of continuity, the second equation

$$\frac{dM_r}{dr} = 4\pi r^2\rho. \quad (2.52)$$

The third is the equation of state as known as the ideal gas law

$$P = \frac{k_B}{m}\rho T, \quad (2.53)$$

the fourth and fifth are the equations of energy transfer, caused by the radiation and convection, respectively

$$\frac{d}{dr}(aT^4) = -\frac{3\kappa\rho}{c}\frac{L_r}{4\pi r^2}, \quad (2.54)$$

$$\frac{dT}{dr} = \left(1 - \frac{1}{\gamma}\right)\frac{T}{P}\frac{dP}{dr}, \quad (2.55)$$

where a is the radiation density constant, c is the speed of light, κ is the gas opacity, L_r is the total energy flux passing through a sphere of radius r , γ is the specific heat ratio.

In general, we cannot solve them analytically because m and κ is complicated. We show two simple solutions using some assumptions.

In the first case we consider the structure of thin atmosphere. We assume that $T = T_0(\text{const.})$, $m = m_0(\text{const.})$, $M_{\text{core}} \gg M_{\text{atm}}$ ($M_r \simeq M_{\text{core}}$, and so thin that we can approximate the gravitational acceleration is a constant $\frac{GM_r}{r^2} \simeq \frac{GM_{\text{core}}}{R_{\text{core}}^2} \equiv g$). In this situation, we can rewrite Equation (2.51) as

$$\frac{dP}{dr} = -\rho g = -\frac{m_0 g}{k_B T_0} P, \quad (2.56)$$

using Equation (2.53) to eliminate ρ . The solution of Equation (2.56) is a exponential function of height,

$$P = P_0 \exp\left(-\frac{m_0 g}{k_B T_0} z\right), \quad (2.57)$$

where z is the radial coordinate relative to the core surface $z = r - R_{core}$, P_0 is the surface pressure

$$P_0 = \frac{M_{atm}g}{4\pi R_{core}^2}. \quad (2.58)$$

The inverse of exponential coefficient $\frac{k_B T_0}{m_0 g} \equiv H$ is the atmospheric scale height. In our Earth, the scale height is $\sim 4km$, which means that the pressure becomes one tenth of the pressure $10km$ below. We can also derive the density profile

$$\rho = \frac{m_0 P_0}{k_B T_0} e^{-z/H} \equiv \rho_0 e^{-z/H}. \quad (2.59)$$

In the second case we continue to assume $m = const.$ and $M_r \simeq M_{core}$, while we discuss the energy transfer more precisely; we consider the radiation only energy transfer and assume that $\kappa L_r = const.$ In fact, the radiative equilibrium is not valid completely in lower layer of atmosphere where the convection occurs, but in the other layer this is a good assumption. From equations (2.51) and (2.54),

$$\begin{aligned} \frac{d}{dP}(aT^4) &= \left(-\frac{3\kappa\rho}{c} \frac{L_r}{4\pi r^2} \right) / \left(-\frac{GM_{core}\rho}{r^2} \right) \\ &= \frac{3}{4\pi cG} \frac{\kappa L_r}{M_{core}} = const. \end{aligned} \quad (2.60)$$

By integrating the equation, we obtain

$$T^4 - T_0^4 = A(P - P_0), \quad (2.61)$$

$$A \equiv \frac{3}{4\pi acG} \frac{\kappa L_r}{M_{core}}. \quad (2.62)$$

If we assume the relation²

$$T^4 = AP, \quad (2.63)$$

and substitute the equation into Equation (2.53), we obtain

$$\begin{aligned} P^4 &= \left(\frac{k_B}{m} \right)^4 \rho^4 T^4 \\ &= \left(\frac{k_B}{m} \right)^4 \rho^4 AP. \end{aligned} \quad (2.64)$$

Substituting the equation into Equation (2.51), the differential equation of ρ is given as

$$\frac{d\rho}{dr} = -\frac{3}{4} \frac{GM_{core}}{r^2} \left(\frac{k_B}{m} \right)^{4/3} A^{1/3} \rho^{2/3}. \quad (2.65)$$

²Now the index 0 is to denote $r = R_{Bondi}$. We assume that $T \gg T_0, P \gg P_0$.

We can solve the approximate solution of Equation (2.65) as

$$\rho \simeq \frac{\pi a c}{48 \kappa L} \left(\frac{G M_{core} m}{k_B} \right)^4 \frac{1}{r^3}, \quad (2.66)$$

and integrating this equation in r , we obtain the total mass of atmosphere

$$\begin{aligned} M_{atm} &= \int_{R_{core}}^{R_{Bondi}} 4\pi r^2 \rho dr \\ &= \frac{\pi^2 a c}{12 \kappa L} \left(\frac{G M_{core} m}{k_B} \right)^4 \log \left(\frac{R_{Bondi}}{R_{core}} \right). \end{aligned} \quad (2.67)$$

Equation (2.67) indicates that the atmosphere mass significantly increases as the core mass increases. Since we assumed that the planet mass is similar to the core mass, Equation (2.67) is not valid when $M_{atm} \gtrsim M_{core}$. However, we do not have to take into account as far as we consider typical-sized terrestrial planets, which have the smaller mass than the critical mass $\sim 10M_{\oplus}$. This estimation of the atmosphere mass is valid for the planets during formation, because we assume that they can directly capture their atmosphere from the stellar nebula. Unlike the gas giant planets, which retain these primary atmospheres, terrestrial planets lose their primary hydrogen-helium-rich atmospheres after formation, and acquire the secondary atmospheres via outgassing, volcanism, or comet impact. Terrestrial planet's atmospheres show a wide diversity due to their gas composition and evolution over billions of years including photochemistry, interaction with the core surface, and atmospheric escape processes.

2.4 General Circulation Model

In this section we briefly the basic physical process of the planetary atmospheric circulation. To describe the cloud pattern of a planet, it is important to calculate in three dimension because the atmospheric circulation which determines the cloud pattern of a planet cannot be represented in lower dimensional calculation. The atmospheric circulation transports the radiative energy around the sphere and determines the thermal and wind structure.

The basic equations are

$$\frac{d\rho}{dt} + \rho \nabla \cdot \mathbf{v} = 0, \quad (2.68)$$

$$\rho \frac{d\mathbf{v}}{dt} + \nabla p + \nabla \Phi = \mathcal{F}, \quad (2.69)$$

$$p = \rho R T, \quad (2.70)$$

$$\frac{dC_p T}{dt} = \frac{1}{\rho} \frac{dp}{dt} + Q, \quad (2.71)$$

$$\frac{dq}{dt} = S_q, \quad (2.72)$$

where ρ , \mathbf{v} , p , Φ , T , q are the density, velocity, pressure, gravitational potential, temperature, specific humidity, R , C_p are the gas constant, specific heat at constant pressure, \mathcal{F} , Q , S_q are the external force, external heat, and vapor source term respectively. The specific humidity q is defined to be the ratio of the vapor mass to the total atmosphere mass:

$$q \equiv \frac{\rho_v}{\rho}, \quad (2.73)$$

where ρ_v is the vapor density.

This three dimensional calculation is difficult to solve analytically. How can we tackle on this problem? The most powerful method is numerical calculation. We briefly introduce the GCM which give the numerical solution of the atmospheric parameters and its evolution of the whole planet.

General Circulation Model(GCM) is a three dimensional numerical model for planetary atmosphere simulation of the whole sphere. GCM provides a time evolution of atmospheric parameters by solving above basal physical equations: hydrodynamics, thermodynamics, radiation. They also take account of the generation/extinction and the motion of clouds, precipitation, water absorption/evaporation into/from the surface, and so on. There are many GCMs developed by research institutes around the world. Although the original GCM was developed for simulation of a climate (weather prediction) of the Earth, these days some GCMs are available for other planets: Mars, Venus, Jupiter, and even some extrasolar planets whose environments we have never seen.

GCMs are often used for the weather forecasting or the future prediction such as the greenhouse effect. Moreover recently they are used in the planetary science, both inside and outside of the Solar system. Takahashi et al. (2003) calculated the Martian atmosphere with their GCM. They reported the asymmetrical circulations between the Northern and Southern hemispheres and some properties which is consistent with Mars observations. Ishiwatari et al. (2002) discussed the runaway greenhouse state of a planet by changing the solar constant on their GCM. They showed that the atmospheric circulation delays to enter the runaway states by transporting incident heat to the polar cold region. In addition, Ishiwatari et al. (2007) reported the snowball and runaway greenhouse planets on their GCM and the existence of multi-equilibrium with the same solar insolation. They also showed that the snowball planet cannot get out easily from the state. Turbet et al. (2017) discussed the habitability of Proxima b reported by Anglada-Escudé et al. (2016) by experimenting the synchronously rotating planet calculation on GCM. They calculated a lot of possible planets with the different atmospheric composition and amount of water.

The important studies for this thesis are Williams & Pollard (2003) and Abe et al. (2005), discussing the obliquity dependence on the planetary climate. Williams & Pollard (2003) reported that highly oblique planets $\zeta \geq 54^\circ$ showed a large temperature difference in a year reaching $80^\circ\text{C} - 100^\circ\text{C}$. Abe et al. (2005) found four different climate

states due to the planetary obliquity and reported that low oblique planets have the similar circulation pattern to that of Earth, governed by the Hadley circulation.

Chapter 3

General Circulation Model

The GCM we use in this thesis is DCPAM5 (the Dennou-Club Planetary Atmospheric Model), which is developed by GFD-Dennou Club¹ for planetary climate modeling². DCPAM5 was developed with the aim of being able to calculate an atmospheric condition of various terrestrial planets, by using general formulae as much as possible, by excluding properties and modules unique to the Earth. DCPAM5 allows us to calculate terrestrial planets, having various orbital parameters, spin parameters, radius, atmospheric composition or amounts, amounts of water, arrangement of land/ocean and so on to some extent. Here we show a brief overview of using equations and physics.

DCPAM5 uses the σ -coordinate system and the primitive equation system. σ -coordinate system uses latitude θ and longitude ϕ as horizontal coordinates, and normalized pressure $\sigma = p/p_s$ as vertical coordinate, where p is the pressure and p_s is the surface pressure of the considered column. DCPAM5 uses the Gaussian grid as the horizontal grid in order to calculate the time evolution of physical quantities by expressing their horizontal equations in the form of spherical harmonic function. This method is called spectral transform method. The Gaussian latitude is defined to be the set of roots $\theta_j (j = 1, 2, \dots, J)$ of the J -th Legendre function $P_J(\sin \theta)$, and the order to be $-\frac{\pi}{2} < \theta_1 < \theta_2 < \dots < \theta_J < \frac{\pi}{2}$, where J is the latitudinal grid number. The Gaussian longitude is defined to be equally spaced,

$$\phi_i = \frac{2\pi(i-1)}{I} \quad (i = 1, 2, \dots, I), \quad (3.1)$$

where I is the longitudinal grid number. DCPAM5 also uses the Lorenz grid as the vertical grid. Under this arrangement of grid, horizontal wind velocities u , v , temperature T , specific humidity q , and tracer mixing ratio of a grid are defined at the center of the vertical layer, while the vertical wind velocity is defined at the boundary of the vertical layer. We number the vertical layer from the bottom layer up. We use half-integers as indices of the boundary, and integers as the center. When the vertical grid number is K , the number of the bottom of the atmosphere (planetary

¹URL: <http://www.gfd-dennou.org>

²We note that the version of the model which we use for the experiment is dcpam5-20161021.

solid/liquid surface) is $\frac{1}{2}$, the number of the top of the atmosphere (upper limit of calculation) is $K + \frac{1}{2}$, and the numbers of the center of the lowest and highest layer are 1 and K , as shown in Fig. (3.1).

In the primitive equation system, we assume that the equation of vertical motion is hydrostatic. This assumption is appropriate in cases where the horizontal dynamical scale is much larger than the vertical one. Furthermore, we assume that these motions are limited in the region near the planetary surface. We carry out calculations in the region up to about 30km in vertical scale, which includes the whole troposphere (0~15km) and a part of the stratosphere (15~50km), while the horizontal scale is about 40Mm. Because clouds are generated in the troposphere of the planet, it is enough box size for our study to express the motion and generation of clouds in Earth twin planets which have the same atmosphere, the same geography, the same insolation, the same orbit, but the different spin obliquities. We here rewrite the basic equations (2.68-2.72) in the term of σ -coordinate system. By changing the coordinates from inertial frame to co-rotating frame³, and changing the variable from z to σ , we obtain

$$\frac{\partial \ln p_s}{\partial t} + \nabla \cdot \mathbf{v}_H + \frac{\partial \dot{\sigma}}{\partial \sigma} = 0, \quad (3.2)$$

$$\frac{du}{dt} - fv - \frac{uv}{a} \tan \theta = -\frac{1}{a \cos \theta} \frac{\partial \Phi}{\partial \phi} - \frac{RT}{a \cos \theta} \frac{\partial \ln p_s}{\partial \phi} + \mathcal{F}_\phi, \quad (3.3)$$

$$\frac{dv}{dt} + fu - \frac{u^2}{a} \tan \theta = -\frac{1}{a} \frac{\partial \Phi}{\partial \theta} - \frac{R^d T_v}{a} \frac{\partial \ln p_s}{\partial \theta} + \mathcal{F}_\theta, \quad (3.4)$$

$$\frac{\partial \Phi}{\partial \sigma} = -\frac{RT}{\sigma}, \quad (3.5)$$

$$\frac{dT}{dt} = \frac{RT}{C_p} \left\{ \frac{\partial \ln p_s}{\partial t} + \mathbf{v}_H \cdot \nabla_\sigma \ln p_s + \frac{\dot{\sigma}}{\sigma} \right\} + \frac{Q}{C_p}, \quad (3.6)$$

$$\frac{\partial q_{cw}}{\partial t} = G + P, \quad (3.7)$$

where \mathbf{v}_H and $\dot{\sigma}$ are the horizontal and vertical wind velocity in σ coordinate system, u , v is the longitudinal and latitudinal wind velocity, a is the radius of planet, f is the Coriolis parameter of planet defined to be $f = 2\Omega \sin \theta$, Φ is the gravitational potential defined to be $\Phi = gz$, \mathcal{F}_λ and \mathcal{F}_ϕ is the longitudinal and latitudinal component of external force and viscous force, ∇_σ is defined to be the differential operator in σ coordinate system, and G and P is the generation rate and extinction rate of

³We only take the spin motion of the planet around its axis into account, not the orbital motion.

water cloud. All extinct clouds drop to the surface as rain and/or snow according to temperature. As boundary conditions, DCPAM5 uses

$$\dot{\sigma} = 0, \quad \text{at } \sigma = 0, 1. \tag{3.8}$$

It means that DCPAM5 neglects the atmospheric absorption/outgassing in the surface and atmospheric escape into the space. It is a reasonable assumption for our study because the atmospheric circulation timescale (~ 10 yrs) is shorter than the quantitative or chemical change timescale ($\sim 10^3$ yrs).

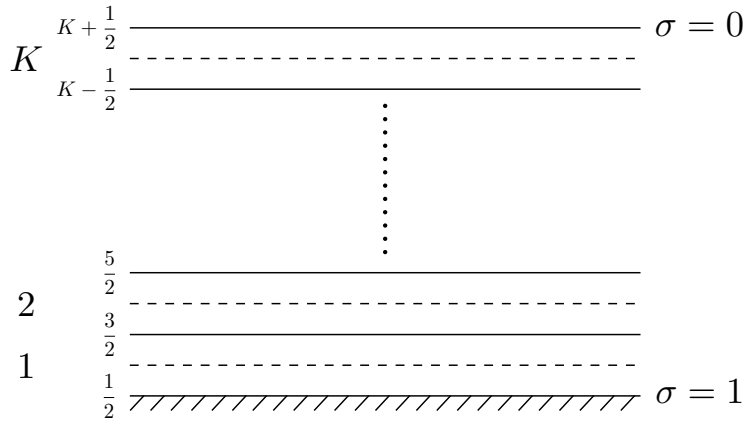


Figure 3.1: Schematic illustration of the vertical grid. In this figure, we assume that the shaded part is the planetary surface, and the dotted and solid lines are the center and boundary of each layer.

3.1 Setup and Sub-grid physical processes

We set the horizontal resolution $I \times J = 32 \times 64$. The vertical σ resolution is $K = 26$, and the position of grid points are discretized by the method of Arakawa & Suarez (1983), as shown in Table 3.1. Their resolutions are the least resolution which can express the global meridional circulations observed in the Earth. The time resolution of experiments are 30 minutes for planets with low obliquities $\zeta < 75^\circ$, 15 minutes for high obliquities $\zeta \geq 75^\circ$. These time resolution is required by the CFL condition, which states that the propagation speed of information should be faster than the physical propagation speed, the speed of sound. It is because the maximum wind speed blowing in a planet with high obliquity is much faster than that in a planet with low obliquity (Williams & Pollard 2003) that we utilize the different time resolutions.

We use some parameterized physical processes. In shortwave (visible and near infrared, corresponding to the range of incident stellar flux) radiation process, we take

account of absorption by H₂O and CO₂, absorption and scattering by clouds, and the Rayleigh scattering. In longwave (mid and far infrared, corresponding to the range of planetary thermal emission) radiation process, we take account of absorption by H₂O, CO₂ and clouds. The level-2.5 closure scheme of Mellor & Yamada (1982) is used for turbulent diffusion. The methods of Beljaars & Holtslag (1991) and Beljaars & Viterbo (1994) are used for surface flux calculation. Moist convection is parameterized by the Relaxed Arakawa-Schubert scheme described in Moorthi & Suarez (1992). Large scale condensation (non-convective condensation) is parameterized by the moist convective adjustment scheme of Le Trent & Li (1991). The bucket model of Manabe (1969) is used for soil moisture calculation. The slab ocean model is used for ocean model: This configuration allows to determine the sea surface temperature by calculating the surface energy flux.

In order to see the obliquity-dependence of the climate of the Earth, we use the parameters of the Earth basically except for planetary obliquity. We also set eccentricity to $e=0$ (Earth: $e = 0.0167$). Table 3.2 shows these parameters and values in our experiments. We do not use observational data such as surface temperature, sea ice concentration, and ozone density, because their distributions are proper to the climate of the Earth which has the obliquity $\zeta = 23.44^\circ$ and they might be different with those of planet with different obliquity. We use observational data of surface geological properties containing orographic height, standard deviation of orographic height, surface roughness index, and surface reflectance index ⁴, which are less independent of climate. Although weathering and cultivation which have proper patterns to the climate of planet can affect their geological properties, we neglect these effects because their timescale to change geological properties ($\sim 10^{2-3}$ yrs) are longer than the thermal timescale (~ 10 yrs). Note that we also use observational data of cloud properties of the Earth; Effective radius of water and cloud particle are $10\mu\text{m}$ and $50\mu\text{m}$, and lifetime of water and ice cloud are 3240 seconds and 8400 seconds. They should be determined by the dynamical convective timescale (Rossow 1978), the timescale in which the size of cloud particle grows up in up-current of air, but in our experiments we cannot follow such cloud microphysics because their timescale is shorter than GCM computational timescale.

3.2 Initial Condition

Now we have to discuss initial conditions for GCM experiments. Because we want to know typical atmospheric circulations and cloud patterns of each Earth twins having different obliquities ($\zeta = 0^\circ, 15^\circ, 30^\circ, 45^\circ, 60^\circ, 75^\circ, \text{ and } 90^\circ$), we have to perform GCM experiments as independent on these initial conditions as possible. Some “violent” initial conditions can reach the multiple statistically quasi-steady states (Noda et al. 2017) or cannot reach any thermal equilibrium states and in case get into runaway greenhouse states or snowball states (Ishiwatari et al. 2007, 2002). On the other hand,

⁴We use the open source `sp_for_Earth.T021.nc`.

the time evolution in GCM makes the memory of initial condition to be almost forgotten; the rotation pattern of a planet can largely determine the annual atmospheric circulation pattern (Abe et al. 2005) after the typical relaxation timescale in which the heat from its star transports to upper atmosphere by atmospheric circulation and thermal structure relaxes (~ 10 yrs).

So we prepare some careful initial conditions for GCM experiments: First we used an isothermal resting atmosphere as the initial condition of $\zeta = 0^\circ$ and 15° . Table 3.3 briefly summarizes the atmospheric parameters and initial values for $\zeta = 0^\circ$ and 15° experiment.

In order to assess the end of relaxation, we use total atmospheric energy as the index of thermal equilibrium. Total atmospheric energy is the sum of kinetic energy $\rho v^2/2$, internal energy $\rho C_v T$, potential energy $\rho g z$, and latent energy $\rho L q$ of the whole atmosphere. Figure 3.2 shows the time variation of total atmospheric energy and annual mean total atmospheric energy. We stop the relaxation runs at 20 years, when the time variation of total atmospheric energy became periodic in one year cycle and the time variation of annual mean total atmospheric energy became smaller than that of 0.1% in last 5 years.

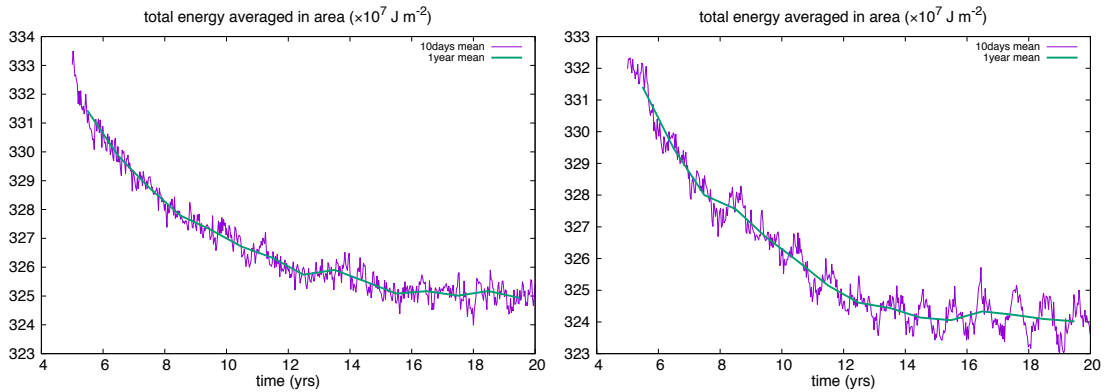


Figure 3.2: The time variation of total atmospheric energy. The left and right panel correspond to the experiments $\zeta = 0^\circ$ and $\zeta = 15^\circ$ respectively. The purple and green line correspond to the value averaged every 10 days and 1 year respectively.

In either case, the long time ($>$ a few years) variation cannot be seen after 15 years⁵. After these first relaxation of 20 years, we calculate each planets for one more model years for use in mock observation. We extract the physical parameters in every

⁵In the case of $\zeta = 0^\circ$ there is no annual periodicity.

grids, averaged every 3 hours, which is the required time resolution for detecting the rotation frequency and its modulation from mock observations.

In the case of planets with higher obliquity, we use the *gradual change technique*. In order to prepare an initial condition of planet $\zeta = 30^\circ$, we perform the extensive 10 years run from the final state of $\zeta = 15^\circ$ calculation, with the setup of planetary obliquity $\zeta = 20^\circ$, the additional $+5^\circ$ degrees, and perform the extensive 10 years run from the final state of $\zeta = 20^\circ$ with the setup of $\zeta = 25^\circ$ again. We use the final state of $\zeta = 25^\circ$ as the initial condition of planet $\zeta = 30^\circ$. By using this technique, we can avoid the turnover of experiments or shorten the relaxation time of planets with high obliquities, which is thought to be longer than that of low obliquity's case. We get initial conditions of planetary obliquity $\zeta = 45^\circ, 60^\circ, 75^\circ$, and 90° in the same way. Figure 3.3 shows the schematic procedure of the *gradual change technique* and our experiments. Every extensive experiments relax and pass the above equilibrium assessment. After these extensive relaxations, where planets relax for 10 years in the obliquities of interest, we calculate each planets for one more model years for use in mock observation.

3.3 Climates of Earth twins with various obliquities

In this section we briefly see the thermal structures of planets in our experiments. Figure 3.4 shows the eastward wind velocity map longitudinal and monthly averaged for October of $\zeta = 0^\circ, 30^\circ, 45^\circ$, and 60° during their 1-year observation runs. The planets $\zeta \leq 45^\circ$ show the two zonal eastward wind in mid-latitude upper atmosphere driven by the Hadley circulation, as known as the jet stream. The planets $\zeta \geq 60^\circ$ (we omit more highly oblique case, but the trend is the same as $\zeta=60^\circ$) shows the equatorial westward wind driven by the circulation from the hot polar region to the cold polar region. These features is consistent with Williams & Pollard (2003) and Abe et al. (2005).

Figures 3.5-3.10 show the temporary averaged water cloud column densities of each months and each oblique planets. The color is unified to the certain range. At first, small oblique planets $\zeta = 0^\circ - 30^\circ$ show a similar cloud distribution over a year, between them. This cloud pattern has three cloudy belts; on the equator and northern and southern mid-latitudes, corresponding to the low pressure zones where the upper stream makes clouds. This pattern becomes weaker as the obliquity becomes larger. The middle oblique planets $\zeta = 45^\circ$ and 60° has global annual thin cloud patterns, except for some seasonal local cloud condensations (e.g., large cloud densities on India, between June and August). Highly oblique planets do also show these locally condensed cloud patterns but their global cloud densities become larger.

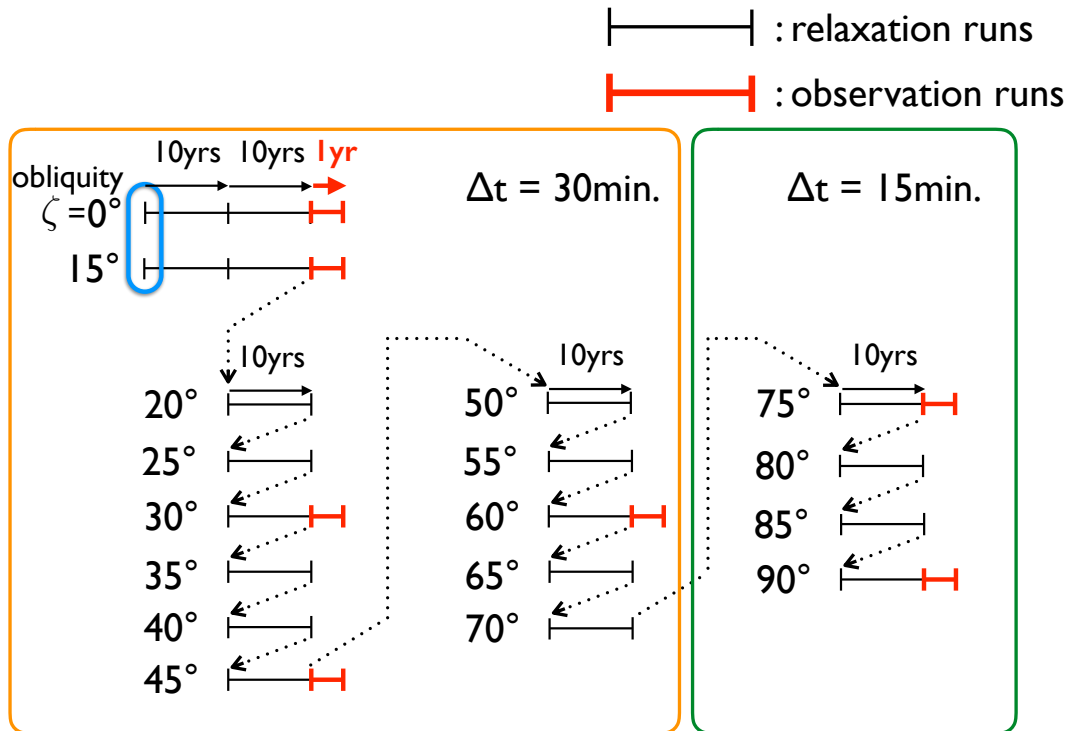


Figure 3.3: Schematic procedure of the *gradual change technique* and our GCM experiments. Values expressed in degrees are planetary obliquities used in experiments. The black thin line segments correspond to relaxation runs and the red bold lines correspond to observation runs. The dotted arrows correspond to the utilization of planetary states for the experiments of a planet with 5° larger obliquity. The blue frame surrounding the left side of line segments of 0° and 15° indicates that the isothermal resting atmospheres are used there as initial conditions. The left and center experiments surrounded by orange frame are performed with 30 minutes time step, while the right experiments surrounded by green are 15 minutes time step.

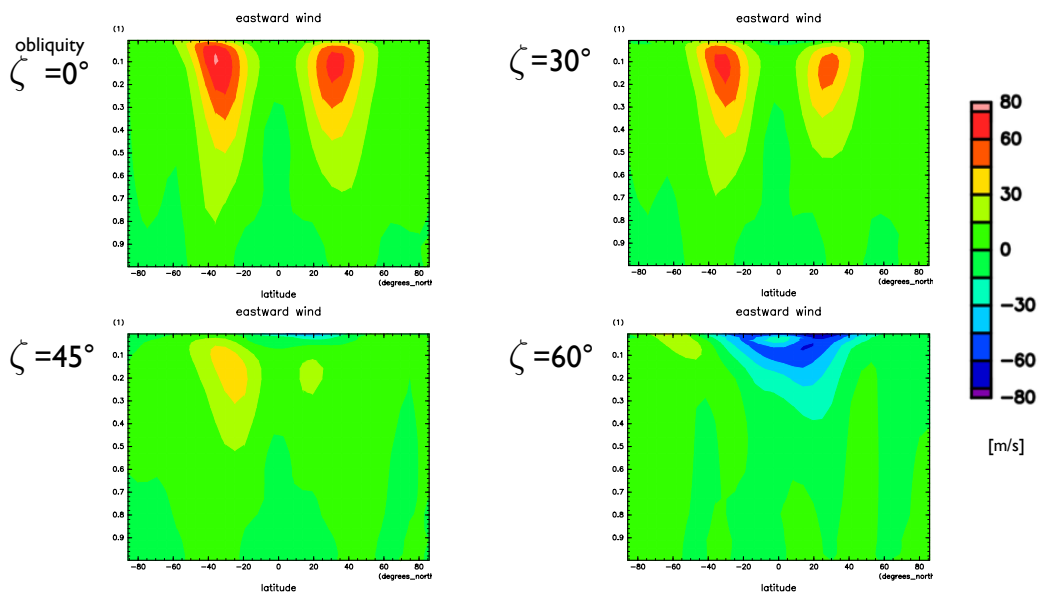


Figure 3.4: Monthly and zonal averaged eastward wind velocity map in October.

Table 3.1: Position of the vertical grid points. k is the index of vertical level, σ_k and $\sigma_{k+1/2}$ are the integer and semi-integer grids, which indicate the center and boundary of calculating level, respectively.

k	σ_k	$\sigma_{k+1/2}$
0		1
1	0.999	0.997
2	0.995	0.993
3	0.987	0.983
4	0.973	0.963
5	0.945	0.928
6	0.911	0.894
7	0.861	0.829
8	0.796	0.762
9	0.729	0.696
10	0.662	0.629
11	0.595	0.562
12	0.529	0.496
13	0.462	0.429
14	0.395	0.362
15	0.329	0.296
16	0.263	0.230
17	0.204	0.179
18	0.159	0.140
19	0.124	0.109
20	9.66×10^{-2}	8.47×10^{-2}
21	7.52×10^{-2}	6.60×10^{-2}
22	5.86×10^{-2}	5.14×10^{-2}
23	4.56×10^{-2}	4.00×10^{-2}
24	3.55×10^{-2}	3.12×10^{-2}
25	2.31×10^{-2}	1.56×10^{-2}
26	6.47×10^{-2}	0

Table 3.2: Values of physical parameters used in the GCM experiments

constants	value [unit]
specific heat at constant pressure of dry air C_p	1004.6 [J kg ⁻¹ K ⁻¹]
gas constant of dry air R	287.04 [J kg ⁻¹ K ⁻¹]
molar weight of dry air m	28.96×10^{-3} [kg/mol]
latent heat of water vapor L	2.5×10^5 [J kg ⁻¹]
lifetime of water cloud	3240 [s]
lifetime of ice cloud	8400 [s]
effective radius of water cloud	10 [μ m]
effective radius of ice cloud	50 [μ m]
planetary radius a	6.37×10^6 [m]
gravitational acceleration g	9.8 [m s ⁻²]
orbital eccentricity e	0.0 [-]
orbital longitude at epoch ϕ_{VE}	279.40 [°]
orbital semimajor axis	1 [au]
solar constant	1366 [W m ⁻²]
spin period P_{spin}	24.0 [hours]
orbital period P_{orb}	365.0 [days]

Table 3.3: Initial values of parameters used in $\zeta = 0^\circ$ and 15° experiments

variable	initial value[unit]
temperature T	280 [K]
surface pressure p_s	1.0×10^5 [Pa]
specific humidity q	0.0 [-]
wind velocity \mathbf{v}	0.0 [m s ⁻¹]

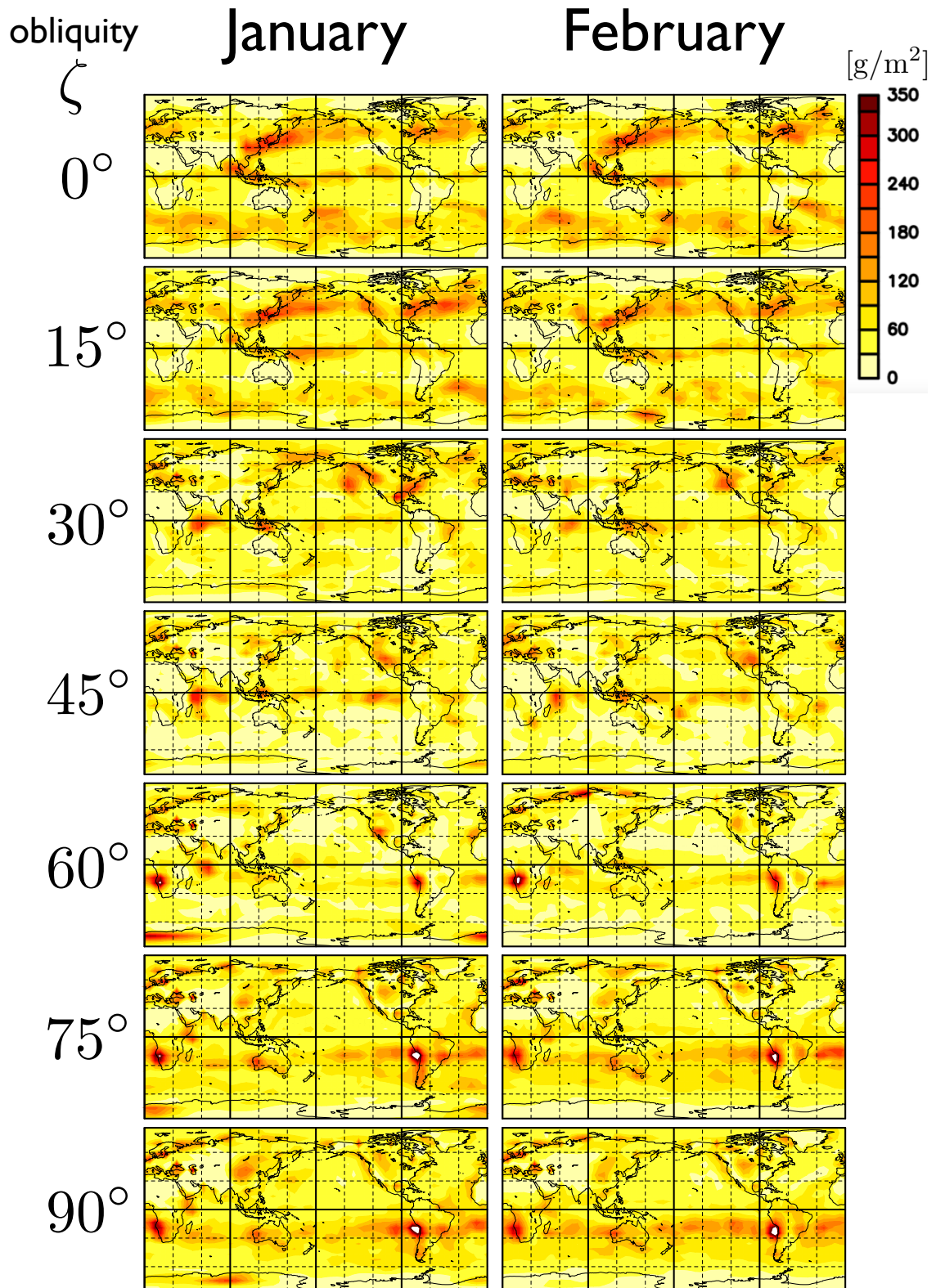


Figure 3.5: Monthly averaged cloud column density map (January and February).

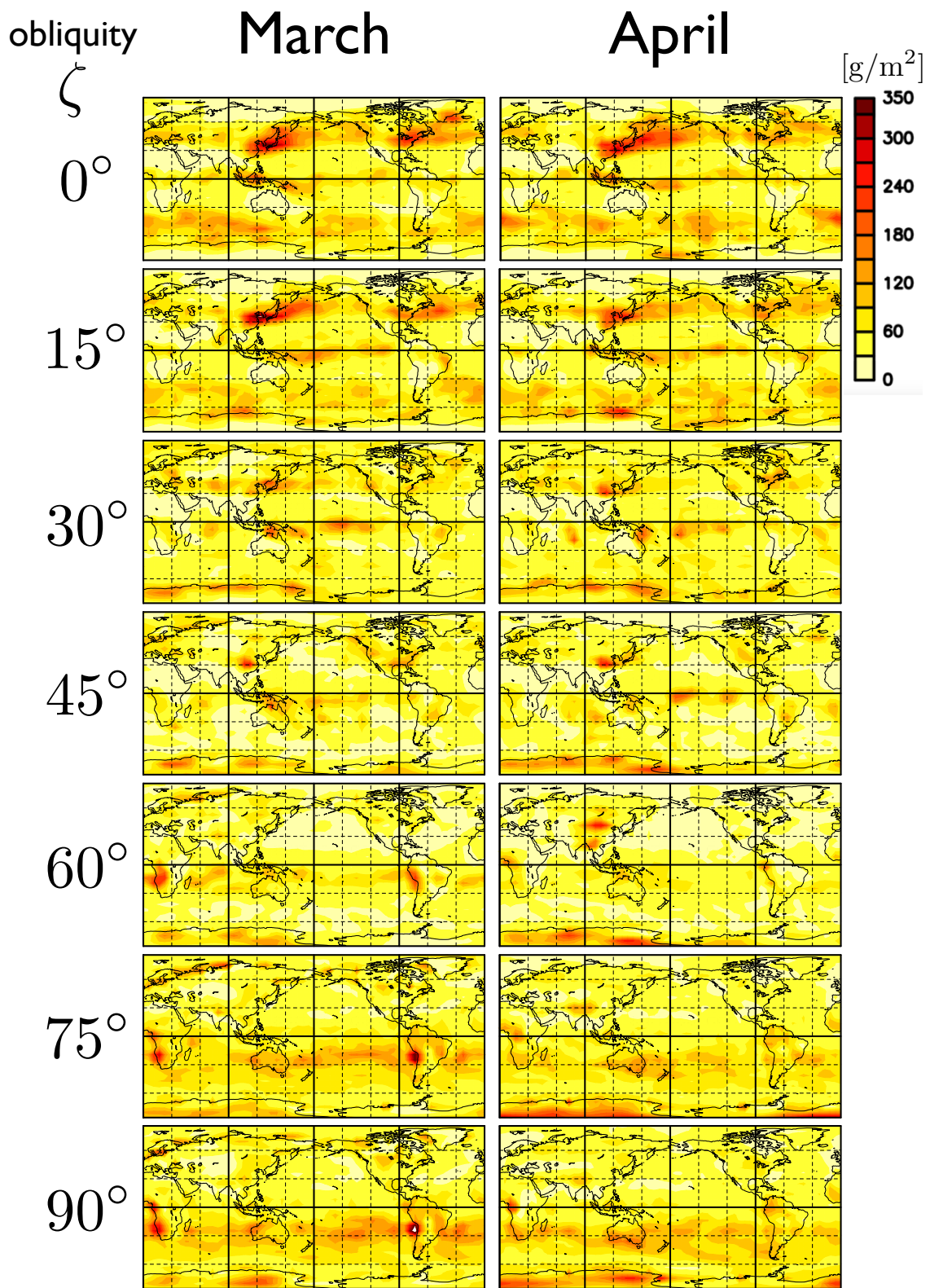


Figure 3.6: Monthly averaged cloud column density map (March and April).

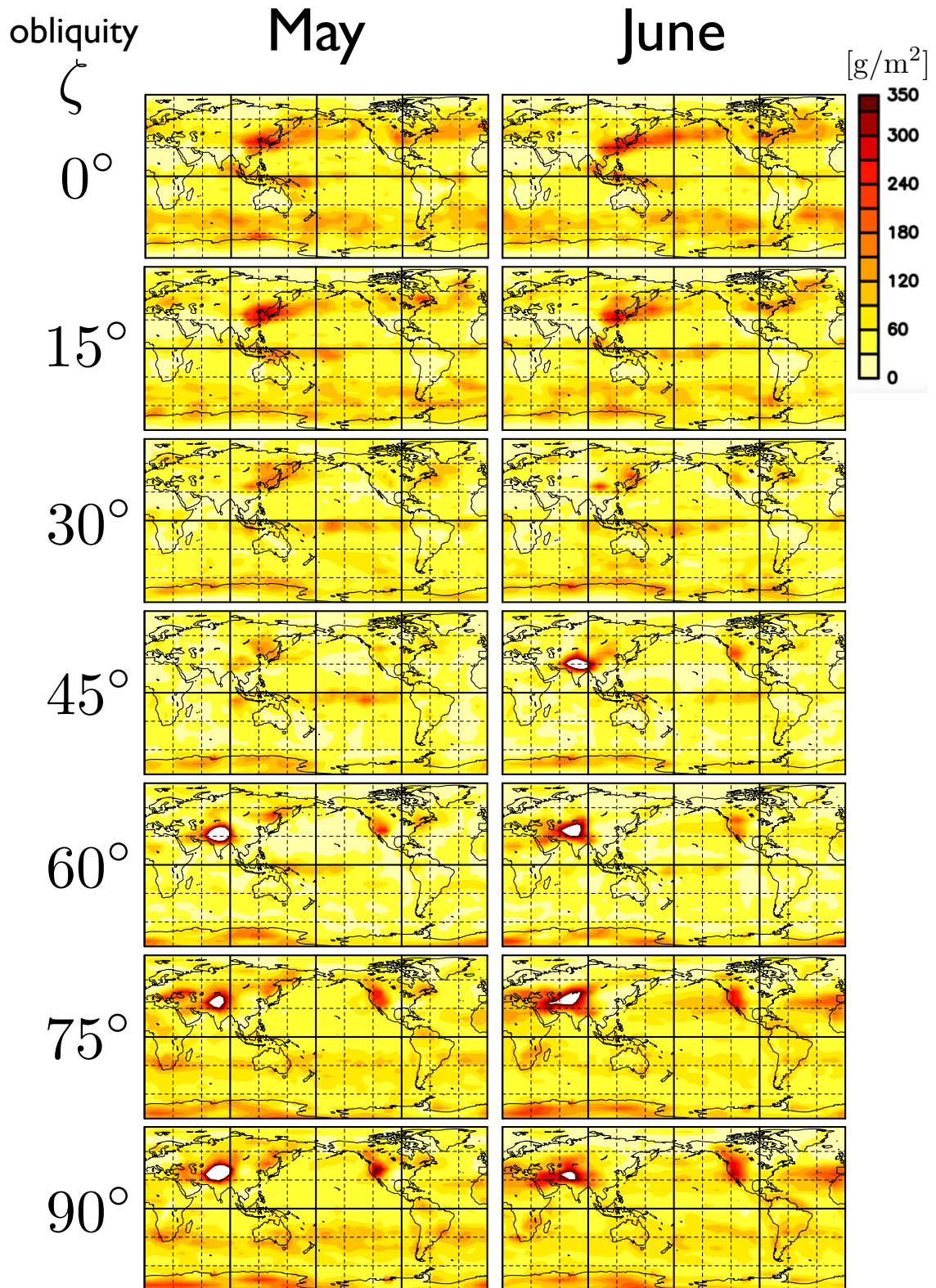


Figure 3.7: Monthly averaged cloud column density map (May and June).

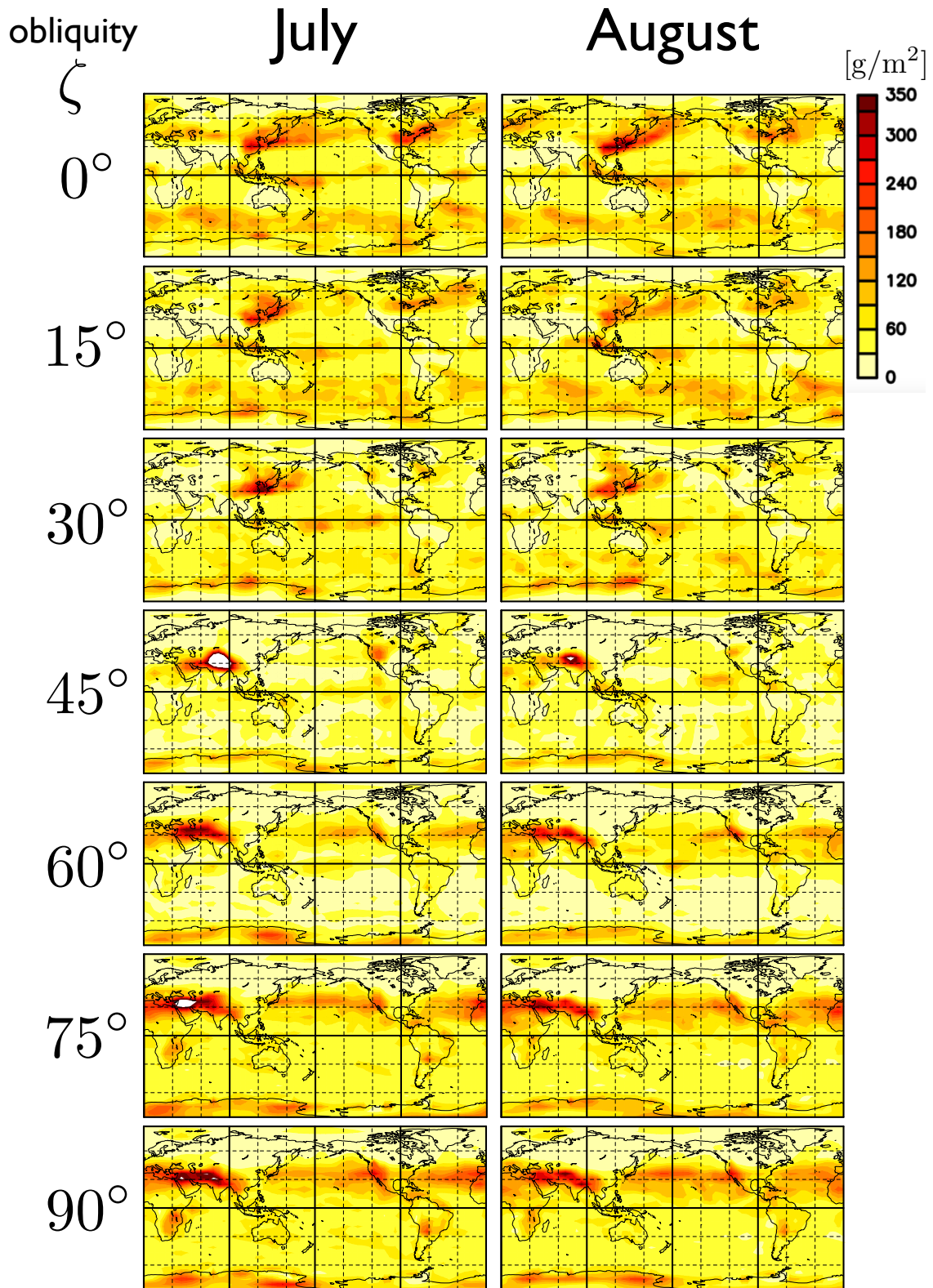


Figure 3.8: Monthly averaged cloud column density map (July and August).

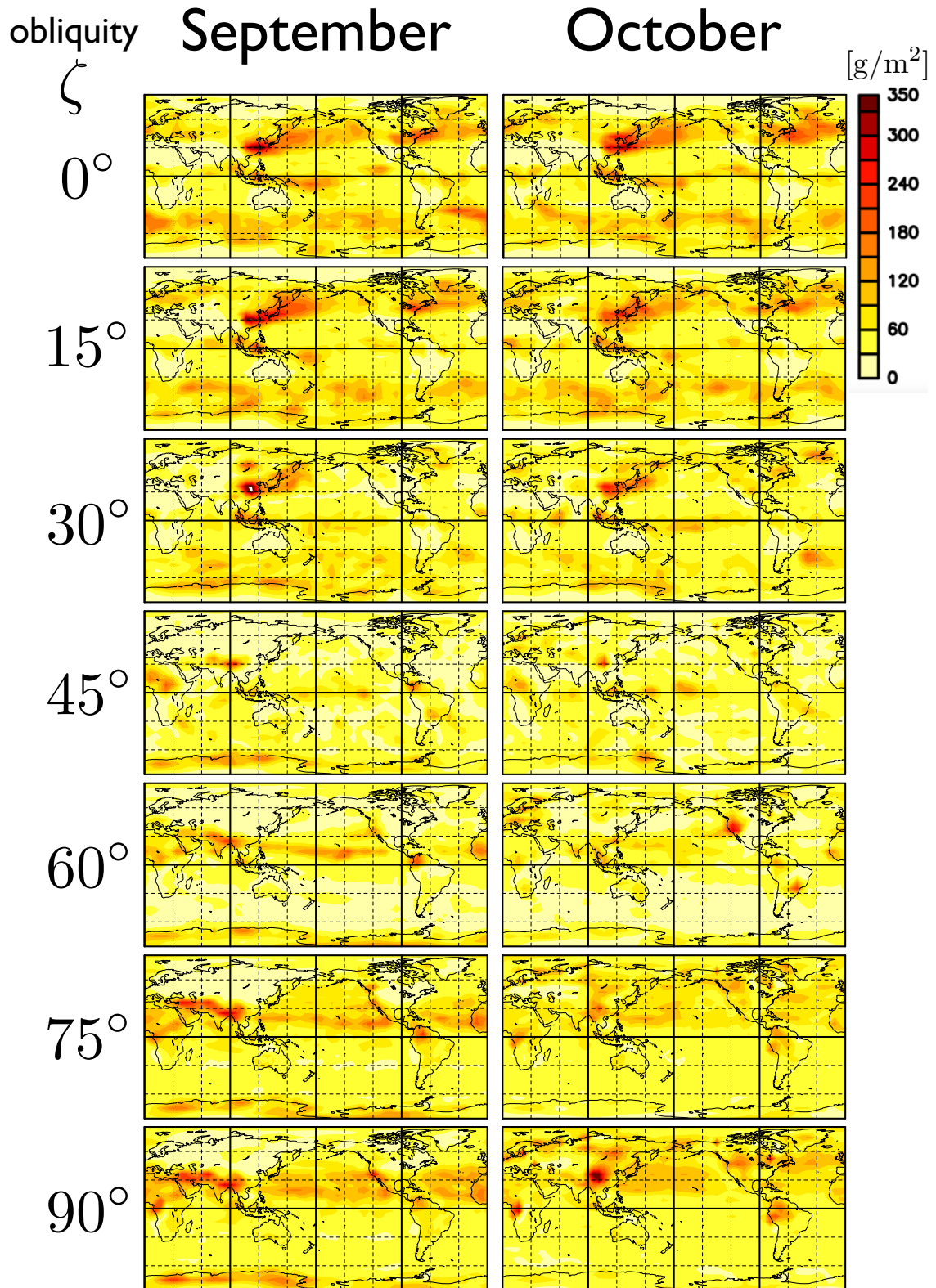


Figure 3.9: Monthly averaged cloud column density map (September and October).

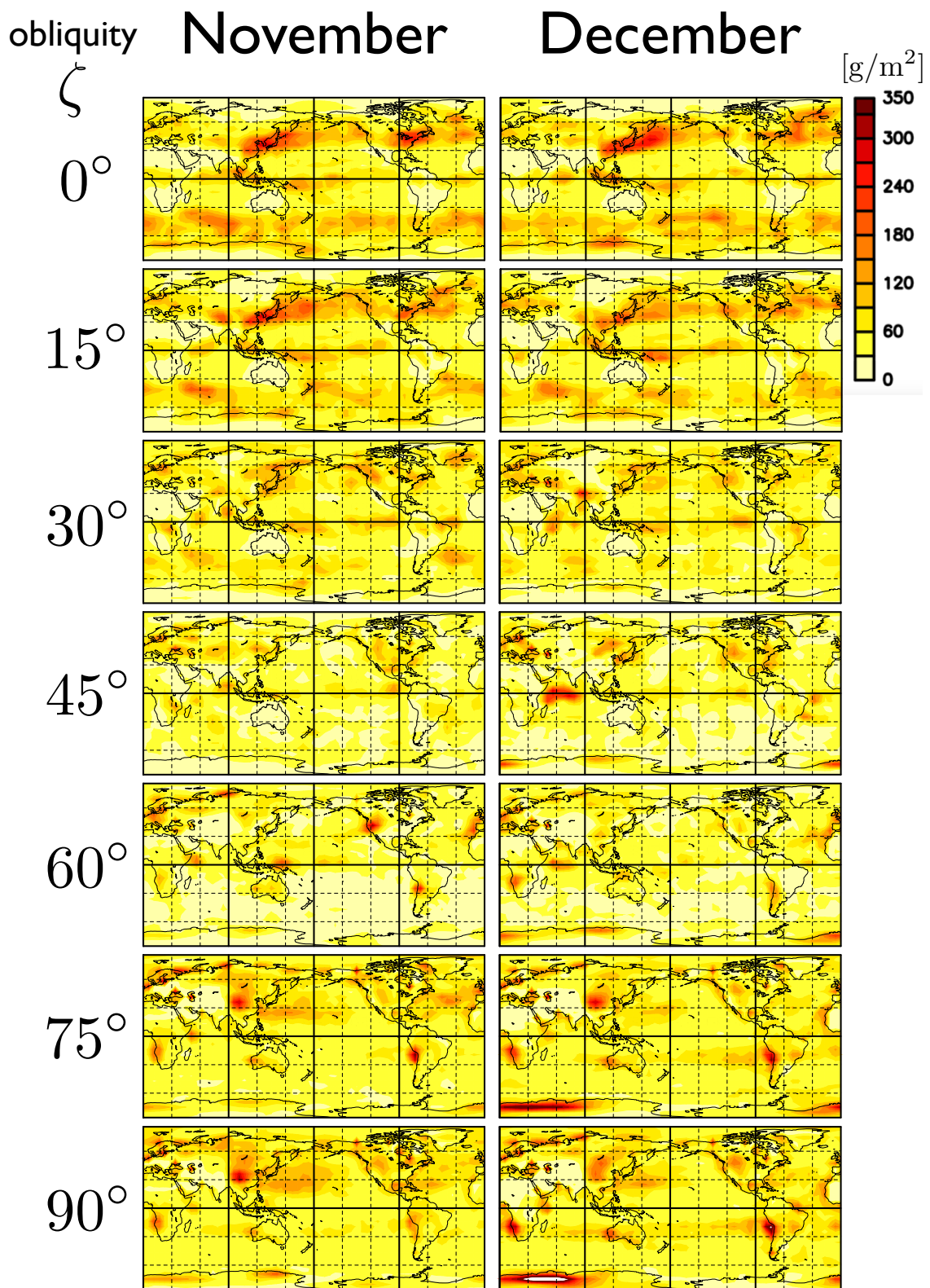


Figure 3.10: Monthly averaged cloud column density map (November and December).

Chapter 4

Mock observation of planets

4.1 Geometric configuration

To generate mock scattered light curves of planets simulated in GCM, we approximate the planetary surface split into 32×64 pixels used in GCM experiments, which is enough to resolve the daily variation of light curves observed every 3 hours. θ_0, θ_1 , and φ are calculated by using the value of (θ_i, ϕ_j) . The area of a surface pixel whose latitude and longitude are (θ_i, ϕ_j) is defined to be

$$S_{ij} = R_p^2 \cos \theta_i \Delta \theta_i \Delta \phi_j, \quad (4.1)$$

where $\Delta \theta_i$ and $\Delta \phi_j$ are defined to be

$$\Delta \theta_i = \begin{cases} (\theta_1 + \theta_2)/2 + \pi/2 & (i = 1) \\ \pi/2 - (\theta_J + \theta_{J-1})/2 & (i = J) \\ (\theta_{i+1} - \theta_{i-1})/2 & (\textit{otherwise}), \end{cases} \quad (4.2)$$

$$\Delta \phi_j = 2\pi/I. \quad (4.3)$$

The total flux of scattered light of a planet is obtained by integrating intensity over the illuminated and visible region of the planetary surface:

$$F(\lambda) = \int_S I(\vartheta_0, \vartheta_1, \varphi; \lambda) \cos \vartheta_1 dS \frac{1}{d^2}, \quad (4.4)$$

and discretizing it, we obtain

$$F(\lambda) = \sum_S I(\vartheta_0, \vartheta_1, \varphi; \lambda) \cos \vartheta_1 S_{ij} \frac{1}{d^2}. \quad (4.5)$$

The scattered intensity of each planetary surface pixel is determined by many complex processes: atmospheric multiple scattering, molecular absorptions, inhomogeneous scattering on the surface, and cloud scattering. In order to tackle them and

obtain the intensity $I(\vartheta_0, \vartheta_1, \varphi; \lambda)$ at each pixel, we use the radiative transfer code libRadtran (Emde et al. 2016; Mayer & Kylling 2005)¹. It include the various detailed modeling of optical properties of the atmosphere, clouds, aerosols, lands, and ocean.

4.2 Model assumption in the radiative transfer calculation

4.2.1 Planetary surface: lands

We utilize the Ross-Li model (Wanner et al. 1995) for the land scattering, the same model as Fujii et al. (2010). This BRDF is represented as a linear combination of three components:

$$f_{\text{land}}(\vartheta_0, \vartheta_1, \varphi; \lambda) = f_{\text{iso}}(\lambda) + f_{\text{vol}}(\lambda)K_{\text{vol}}(\vartheta_0, \vartheta_1, \varphi) + f_{\text{geo}}(\lambda)K_{\text{geo}}(\vartheta_0, \vartheta_1, \varphi). \quad (4.6)$$

The first term is the isotropic (Lambertian) component. The second term is the volume-scattering term, representing the effect of the thick body. The third term is the geometric-optics term, representing the effect of shadow.

A remote sensing project MODerate resolution Imaging Spectroradiometer (MODIS; Salomonson et al. 1989) provides the Ross-Li coefficients of the Earth from their observation data. In this thesis, we use their data set “snow-free gap-filled MODIS BRDF Model Parameters”. This data set includes only the data for lands not oceans and polar region. Their values are monthly and spatially ($0^\circ.05 \times 0^\circ.05$) averaged. We employ the data of March and the center of each pixel. Since the Ross-Li BRDF sometimes has the negative value in certain directions, we calculate them in advance and set to 0 if it becomes negative.

4.2.2 Planetary surface: ocean

As mentioned above, the data set “snow-free gap-filled MODIS BRDF Model Parameters” has no Ross-Li parameters (f_{land} , f_{vol} , f_{geo}) for ocean pixels nor for polar region. We set these pixels as ocean.

We utilize the ocean reflection BRDF model of Nakajima (1983), also the same as Fujii et al. (2010) and employed in the libRadtran. This model considers the specular reflection of the ocean surface (ocean glint), with the small perturbation generated by the wind. Therefore, the ocean BRDF has a parameter of the wind speed. In our simulation, we adopt the wind speed at 10m height above the surface $u_{10} = 4 \text{ m s}^{-1}$, not the wind speed calculated in GCM experiments for simplicity. In the libRadtran, this ocean BRDF model is not suitable for the region outside of specular reflection and f_{ocean} sometimes becomes negative. We set f_{ocean} to 0 wherever the scattered angle is far different from the reflection angle of a mirror surface. For simplicity, we evaluate

¹We use the version 2.0.1 of libRadtran.

whether the pixel is inside of specular reflection or not by the following formula:

$$(\pi - \varphi)^2 + (\vartheta_0 - \vartheta_1)^2 < \left(\frac{\pi}{4}\right)^2. \quad (4.7)$$

4.2.3 Atmosphere and clouds

We use a plane-parallel approximation at each pixel for the calculation of the atmospheric scattering and molecular absorptions because our GCM pixel size is horizontally small and vertically thin. We adopt the DIScrete-ORdinate-method Radiative Transfer model (Stamnes et al. 1988). It solves the radiative transfer in a plane-parallel approximation, by vertically discretizing the atmospheric layer. The governing equations are

$$\begin{aligned} -\mu \frac{dI(\tau, \mu_1, \phi_1)}{d\tau} = & I(\tau, \mu_1, \phi_1) \\ & - \frac{\omega(\tau)}{4\pi} \int d\phi' \int d\mu' p(\tau, \mu_1, \phi_1; \mu', \phi') I(\tau, \mu', \phi') \\ & - (1 - \omega(\tau)) B(T(\tau)) \\ & - \frac{\omega(\tau) I^0}{4\pi} p(\tau, \mu_1, \phi_1; \mu_0, \phi_0) e^{-\tau/\mu_0}, \end{aligned} \quad (4.8)$$

where τ is optical depth, μ_1 and ϕ_1 is the direction of interest, I is intensity, p is scattering phase function, $\omega(\tau)$ is single scattering albedo, $B(T)$ is the Planck function at temperature T , and I^0 is the direct beam from its star observed before incident to the atmosphere. The first term represents the extinction (scattering and absorption), the second term represents the scattering into the direction of interest, the third term represents the thermal emission, and the fourth term represents the scattering of direct ray from the host star. The optical properties of cloud is modeled by the method of Hu & Stamnes (1993), which is parameterized by the effective radius of cloud particle. We also adopt the effective radius of water cloud particle $10\mu\text{m}$ as well in GCM experiments.

To calculate the intensity at the top of atmosphere, this model needs the vertical profile of atmosphere and clouds. We use the GCM data for the configuration: water cloud density, ice cloud density, temperature, air density, and vapor mixing ratio. This code use the profile of these values as a function of altitude starting from the planetary surface which is the position denoted by semi-integer, while the GCM data are defined on the center of grid denoted by integer, as shown in 4.1. Thus, we interpolate the physical values on the boundary of grid: if $1 \leq k \leq K - 1$, the temperature is

$$T_{k+1/2} = \alpha_{k+1/2} T_k + \beta_{k+1/2} T_{k+1}, \quad (4.9)$$

$$\alpha_{k+1/2} = \frac{\log \sigma_{k+1/2} - \log \sigma_{k+1}}{\log \sigma_k - \log \sigma_{k+1}} \quad (4.10)$$

$$\beta_{k+1/2} = \frac{\log \sigma_k - \log \sigma_{k+1/2}}{\log \sigma_k - \log \sigma_{k+1}}, \quad (4.11)$$

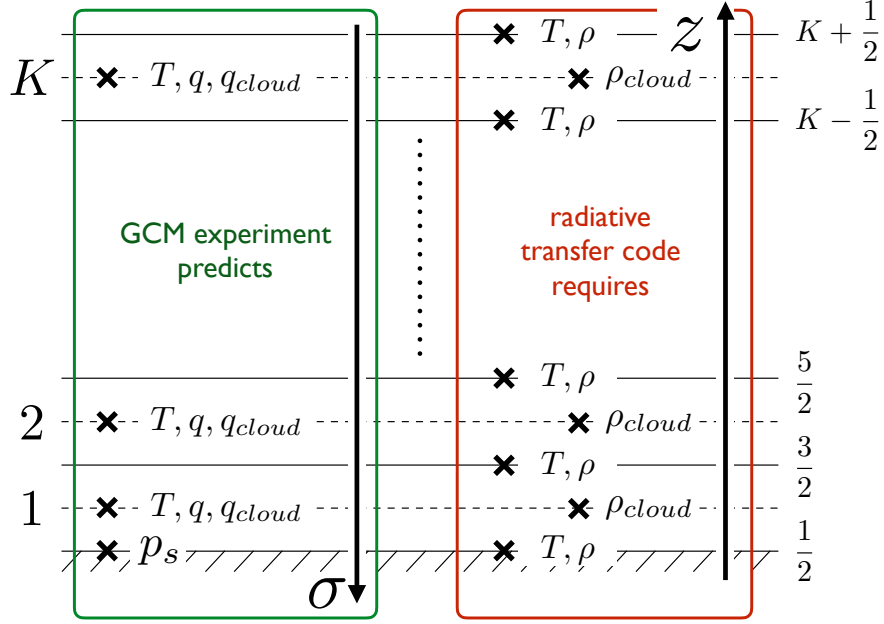


Figure 4.1:

and

$$T_{1/2} = T_1, \quad (4.12)$$

$$T_{K+1/2} = T_K. \quad (4.13)$$

It is a linear interpolation to the logarithmic pressure. The interpolation of vapor mixing ratio is the same as the above method. The density is given by $T_{k+1/2}$ and $p_{k+1/2}$,

$$\rho_{k+1/2} = \frac{p_s \sigma_{k+1/2}}{RT_{k+1/2}}. \quad (4.14)$$

We set the densities of tracer gases CO_2 , O_2 , and NO_2 by using the mixing ratio data of the *US standard atmosphere* provided by Anderson (1986). We linearly interpolate them with altitude. The altitude is defined recursively by

$$z_{k+1/2} = z_{k-1/2} + dz_k, \quad (4.15)$$

$$z_{1/2} = 0, \quad (4.16)$$

$$dz_k = -\frac{dP_k}{\rho g} = \frac{(\sigma_{k-1/2} - \sigma_{k+1/2})RT_k}{\sigma_k g}. \quad (4.17)$$

The cloud density used in this code is the averaged one between layer and layer, that is, the integer grid in GCM experiments. Note that we regard either water or ice cloud as water cloud in order to reduce the computational cost. We obtain the cloud density

$$\rho_{\text{cloud},k} = \frac{(q_{wc,k} + q_{ic,k})p_s \sigma_k}{RT_k},$$

where q_{wc} and q_{ic} are the mixing ratio of water and ice cloud.

4.2.4 Setup

For simplicity we set the observer at the top of GCM vertical grids. While the atmosphere ends up to the region of a few planetary radius, the atmosphere outside of the observer is sparse enough not to affect our results. We assume that the observed intensity is determined only by their radiative transfer calculation in the planetary atmosphere. We set the observer at the direction of inclination $i = 0^\circ$ ². We start the mock observations from the beginning of the GCM observation runs. We take snapshots every 3 hours and multiply the exposure time: we do not the gradual change of the planetary image in order to reduce the computational cost.

We observed the planets in the MODIS photometric bands because the land BRDFs we employed are based on the observations in these bands.

This band selection follows Fujii et al. (2010). The wavelength and width of these bands are shown in Table 4.1. The MODIS project selected their photometric bands so

Table 4.1: MODIS bands we employ

band number	wavelength
1	0.459-0.479 μm
2	0.545-0.565 μm
3	0.620-0.670 μm
4	0.841-0.876 μm
5	1.230-1.250 μm
6	1.628-1.652 μm
7	2.105-2.155 μm

as to characterize the reflection properties of the Earth’s surface by remote sensing: In visible region, they chose 3 bands in order to distinguish between soil, vegetation, and ocean, roughly corresponding to the visible color of red, green, and blue, as shown in Figure 4.2. The vertical axis is the albedo of each surface components. The horizontal axis is the wavelength. In the leftmost visible region (400-700nm), although it is small, they show the different albedo pattern. They also chose 4 near-IR bands in the window of atmosphere, highly transmitting ranges, as shown in Figure 4.3. The wide absorption bands shown in the near-IR region (700-2200nm) are mainly caused by H₂O.

We only compute the intensity at the central wavelength of each band for reducing computational costs. We also make other several mock photometric light curves with different planetary surface configurations; “landless but cloud” and “cloudless but land”. For simplicity we remove lands or clouds from the radiative transfer model and replace zero-albedo surface or atmosphere. We do not perform any additional calculation from the GCM for these configurations.

²Another geometric parameter Θ_{eq} is indefinite because it degenerates.

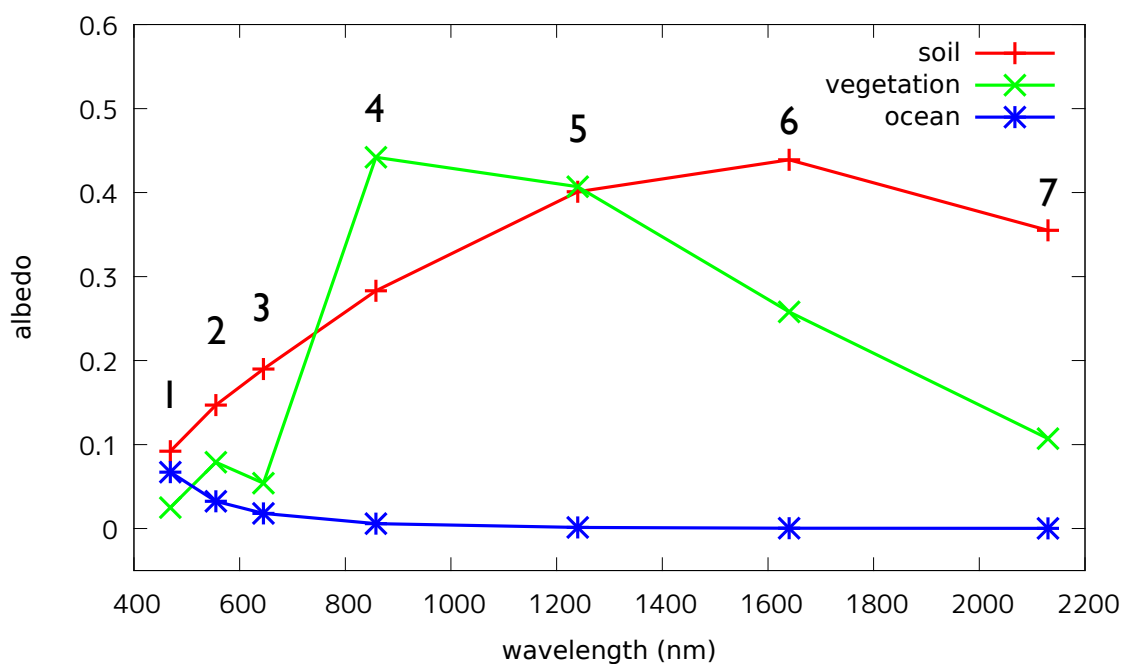


Figure 4.2: Albedo of surface components; soil (red), vegetation (green), and ocean (blue). The positions of points shows the wavelength of the MODIS photometric bands, and the numbers above them are the band number we employed.

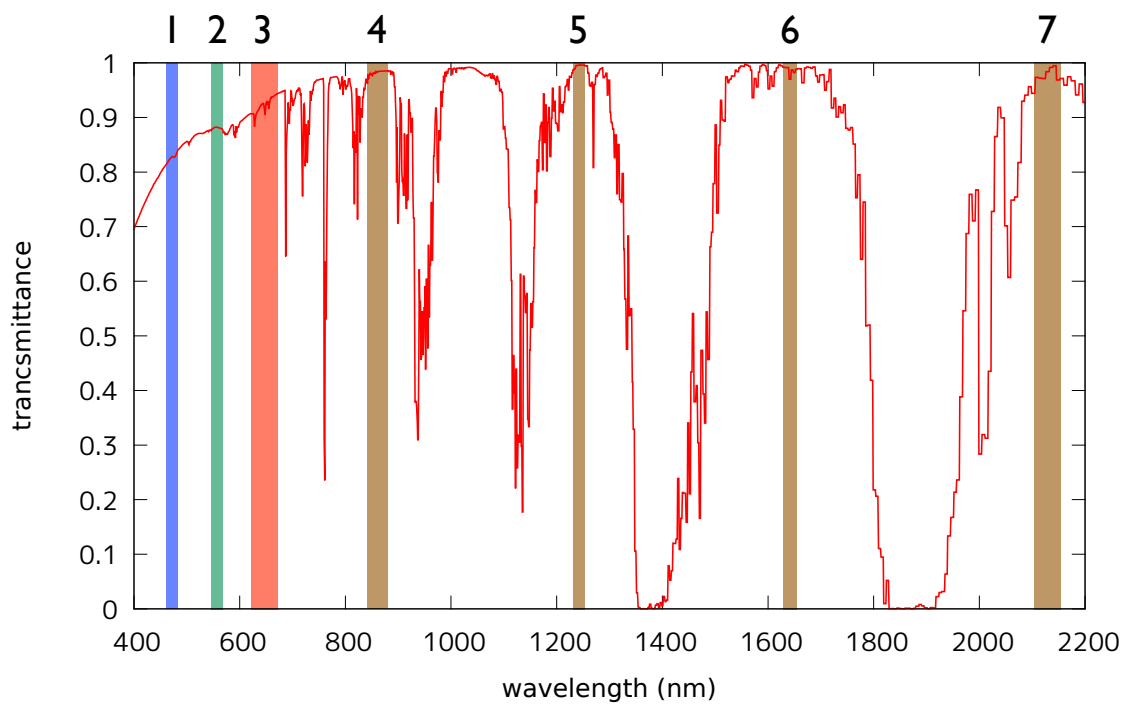


Figure 4.3: Transmittance of the Earth's atmosphere and positions of the MODIS photometric bands.

Actually we have never finished the mock observations completely because of their large computational cost. We preferentially calculate the light curves of $\zeta = 0^\circ$ or those of the band 1. Table 4.2 shows the configuration of light curves already obtained by the radiative transfer calculation.

Table 4.2: Configuration of the radiative transfer calculation already done

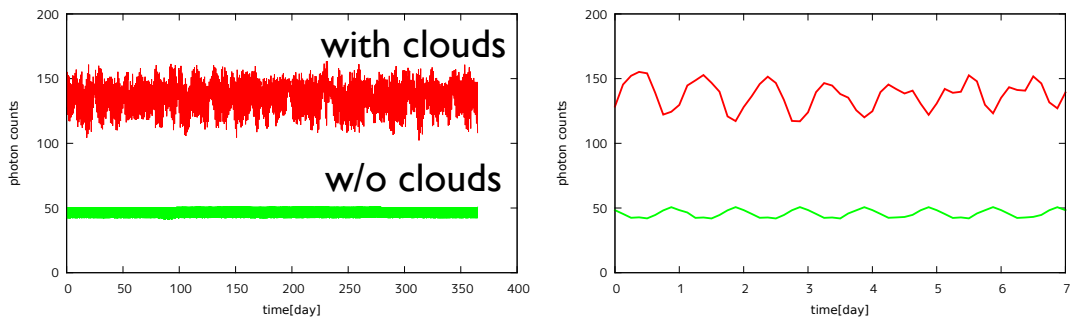
obliquity ζ	bands	clouds	lands
0°	1-7	yes	yes
0°	1-7	no	yes
0°	1	yes	no
15°	1-7	yes	yes
30°	1	yes	yes
30°	1	no	yes
45°	1	yes	yes
60°	1	yes	yes
75°	1	yes	yes
90°	1	yes	yes

4.3 Light curves and images of Earth twins

In this section we briefly see the light curves and images obtained our radiative transfer calculation (although the latter will not be seen by the observer). In all figures showing the light curves, the vertical axis are based on the photon counts assuming an ideal observational condition; 2m telescope diameter 10pc away, completely occulted the host star (no other sources), no instrumental errors. We omit the error bar on photon counts caused by the poisson noise from them because the aim of this thesis is the the planetary obliquity estimation or limitation via the time-frequency analysis itself, not the determination of the sufficient instrumental performance for them. In all figures showing the apparent image of the planet, the colors are the intensity [$\text{mW m}^{-2} \text{nm}^{-1}$]. We add the cloud density map and the albedo map at the same time to the figures.

Figure 4.4 show the light curve of band 1 (upper) and band 7 (lower) over a year (left) and the first 1 week (right) for $\zeta = 0^\circ$. The upper red and lower green lines in each panel are the light curve of the planet with clouds and without clouds. The light curve of the cloudy planet has the non-periodic amplitude variation caused by the dynamical motion of clouds, while the cloudless planet shows quite a periodic light curve. The light curve of the cloudy planet has also three times larger photon counts than the cloudless planet because of the high reflectance of clouds. The 1 week light curve of band 1 slightly shows the periodicity corresponding to the 1 day period while being modulated day by day. On the other hand, that of band 7 is hard to see the periodicity. We will discuss the band dependence of their periodicity with the time-frequency representation in the following chapter.

band 1



band 7

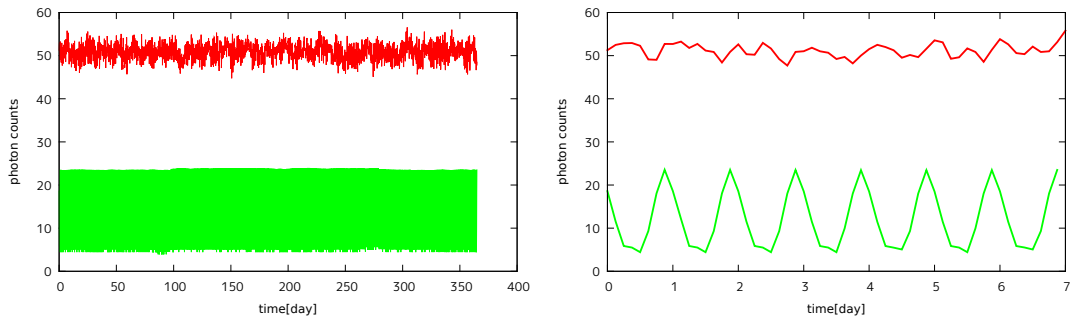


Figure 4.4: Light curves of band 1 (upper) and band 7 (lower) over a year (left) and the first 1 week (right) for $\zeta = 0^\circ$. The upper red and lower green lines in each panel indicate the planet with clouds and without clouds. The cloudy planet shows the quasi-periodic 1 day cycle in the band 1 light curve.

Figure 4.5 shows the planetary image of band 1-7, cloud column density, and albedo at 0.0 day of the observational run. The color of the planetary image indicates the intensity of each grid. The color of the cloud column density and the albedo are the unit of $[\text{g m}^{-2}]$ and non-dimensional value (based on the Lambertian scattering). The line from the center to the right of each panel indicates the prime meridian of the planet and now the star illuminates the planet from the direction. Note that their image are not the expanded map but the apparent image by the observer $i = 0^\circ$. We dare to saturate the color map of the cloud density because the reflectance of clouds reaches the ceiling with the cloud density, more correctly with its optical depth. We show the albedo map in order to only describe the geographical configuration. First of all the intensities are almost proportional to the stellar flux decreasing with wavelength in this range. The intensity maps of 7 bands show almost the same patterns, mainly corresponding to the clouds pattern multiplying with the stellar geometry, $\cos \vartheta_0$. As the band becomes red, the land (the African continent, at the upper right edge of the planet) can be seen because the land has a red albedo (e.g., MODIS observation: Salomonson et al. 1989). We also recognize the band dependence on the contrast of clouds: The bluer the band is, the photometric contrast between dense clouds and relatively sparse clouds. We do not have the explanation for it.

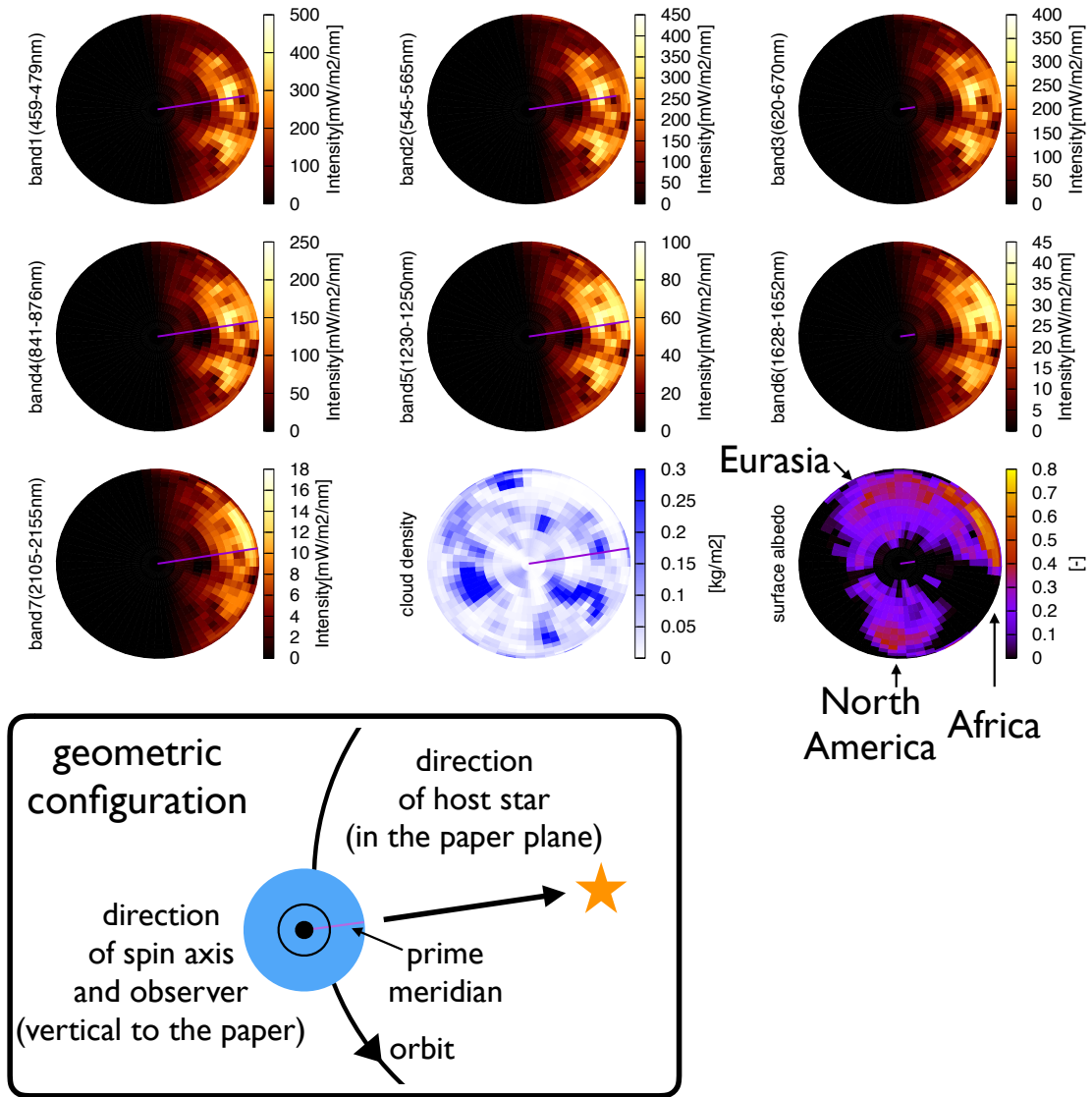


Figure 4.5: The comparison of the apparent image of the planet in 7 bands with the cloud density map and the albedo map. The planet is illuminated from the right and we view from the direction of north pole. All photometric image show the contribution of clouds while the land contribution are shown in only those of redder bands.

Chapter 5

Time-frequency analysis of light curves

5.1 Setup of the time-frequency representation

In order to generate the instantaneous frequency for the estimation of the planetary obliquity, our analytic method in this thesis basically follows Kawahara (2016). We use the computation code for time-frequency representation developed and uploaded by H. Kawahara ¹. Let us describe the details of our time-frequency analysis.

We have 2920 data points in each light curve, corresponding to the observation shot every 3 hours over 1 year ($24 \times 365 / 3 = 2920$). After adding Gaussian noises $\sigma_n = 0$ and σ_s , we divide the data into 73 sets containing 40 data points (~ 5 days) and suppress the amplitude modulation of the light curves by the method described in 2.2.2. The size of data set is determined to be small enough to suppress the amplitude modulation and to be large enough not to follow the apparent periodicity itself. We set the width of Hamming window $\omega = 1/4$ year. We calculate $g(f, t)$ in the range of $[f_m, f_M] = [0.98, 1.02]$ (day^{-1}), with the resolution of $\Delta f / \delta f = 1024$, where $\Delta f = f_M - f_m$ is the frequency range of interest and δf is the computational resolution of frequency. To compute them, we adopt the non-uniform FFT scheme (Greengard & Lee 2004) utilized by Kawahara (2016). We also use Equation (2.45) to extract the instantaneous frequency.

5.2 Band dependence on the time-frequency representation

We briefly show the band dependence on the time-frequency representation. Figure 5.1 shows the time-frequency representation of the 7 band light curves of the no noise case for $\zeta = 0^\circ$, $i = 0^\circ$. The vertical axis is the frequency (day^{-1}) and the horizontal axis is the time (day). The colors show the normalized absolute value of $g(f, t)$. As seen in the

¹<https://github.com/HajimeKawahara/juwvid>

figure, the bluer the band is (the smaller the band number is), the more clearly it shows the ridge of the time-frequency representation. We extract the instantaneous frequency of them shown by the red lines in Figure 5.2. We also draw the input value of frequency modulation calculated by the maximum weighted longitude approximation (constant, 1.0 day^{-1}) by the gray lines. The bands 1-4 still show the continuous modulation of the ridge, while the bands 5-7 have many leaps of the extracted instantaneous frequency over the time. Nevertheless the extracted instantaneous frequencies of band 1-4 are modulated with a long period to some extent, they still trace the input frequency. We discuss the fitting of the extracted instantaneous frequencies with the maximum weighted longitude approximation model in the following section. They also show the band dependence: the bluer the band is, the less it shows the short-period frequency modulation in them.

Figure 5.3 show the instantaneous frequencies of the band 1 light curves of the planet with lands and clouds (red), without lands (gray), and without clouds (black). The landless planet shows almost the same modulation over a year with that of the fully planet, while the cloudless planet shows the less modulation. Thus, we identify the main cause of the frequency modulation as the dynamical effect of clouds by the above comparison. The same fact that the clouds can modulate the instantaneous frequency are seen in other bands or in another observation $\zeta = 15^\circ$. but we do not conclude like this because the acceleration or deceleration of the apparent periodicity is not described by the detailed dynamical motion of clouds. We also have less information of the light curves of highly oblique planets. We postpone the description of the frequency modulation by the detailed dynamical motion of clouds and the frequency modulation of highly oblique planets to a future work.

5.3 Effects of noises on the time-frequency representation

Hereafter we only use the band 1 light curves and its extracted instantaneous frequency as the representative. We briefly show the effect of noises on the time-frequency representation. Figure 5.4 shows the instantaneous frequency of the planetary light curves with different noise amplitudes, $\sigma_n = 0$ and σ_s . Other parameters of the planet and observation are band 1, $\zeta = 0^\circ$. The red and blue lines are the extracted instantaneous frequency of $\sigma_n = 0$ and σ_s . As expected, the noisy signal shows the more noisy frequency modulation than that of the noiseless signal. Nevertheless, the long period modulation caused by the dynamical clouds are also seen in it. This is the strong point of the time-frequency analysis because the statistical noises have less effects on the frequency modulation as discussed by Kawahara (2016).

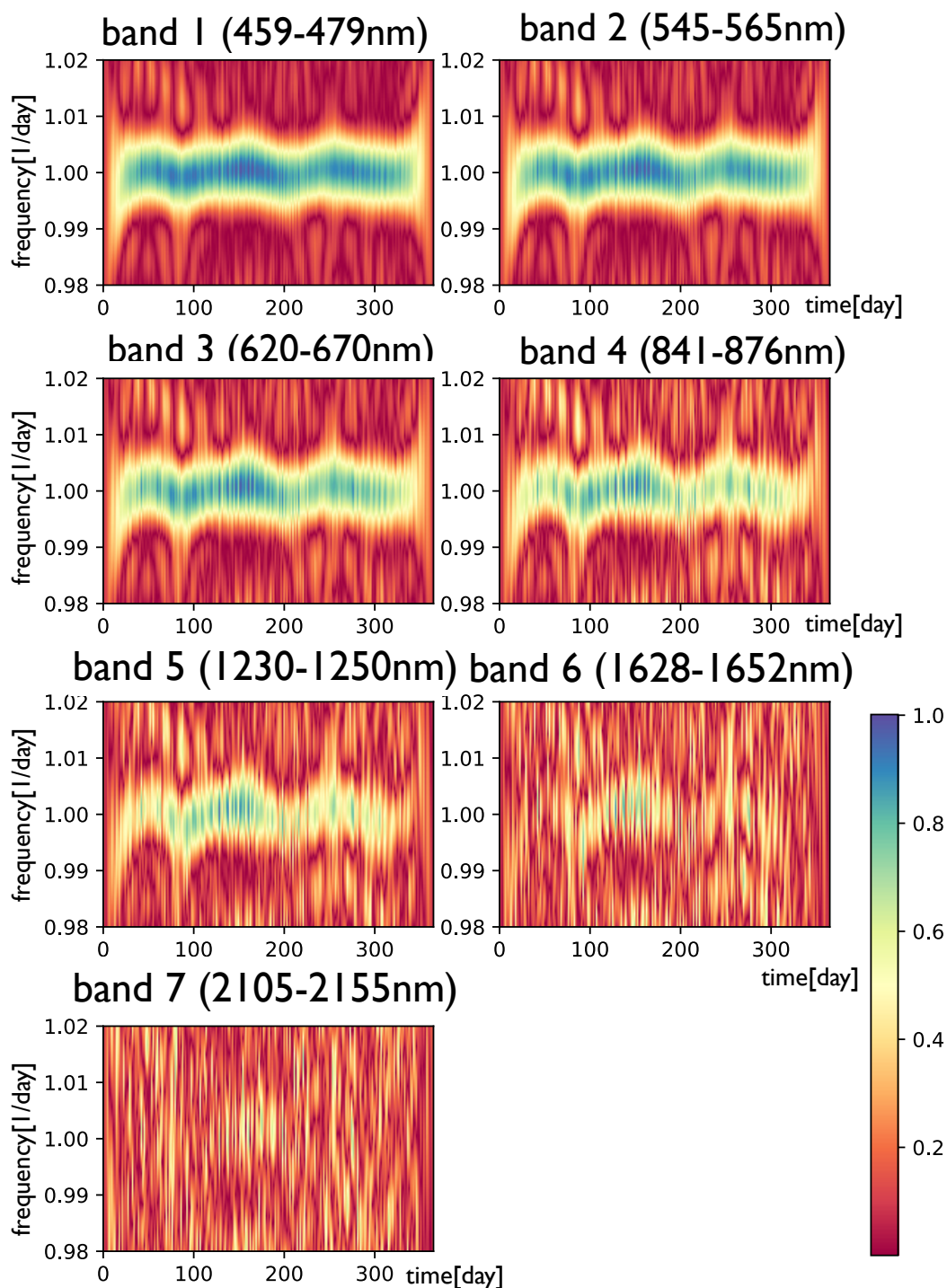


Figure 5.1: The time-frequency representation by the pseudo-Wigner distribution of $\zeta = 0^\circ$, $i = 0^\circ$, and $\sigma_n = 0$. The clear ridge are shown in the upper 4 panels, band 1-4.

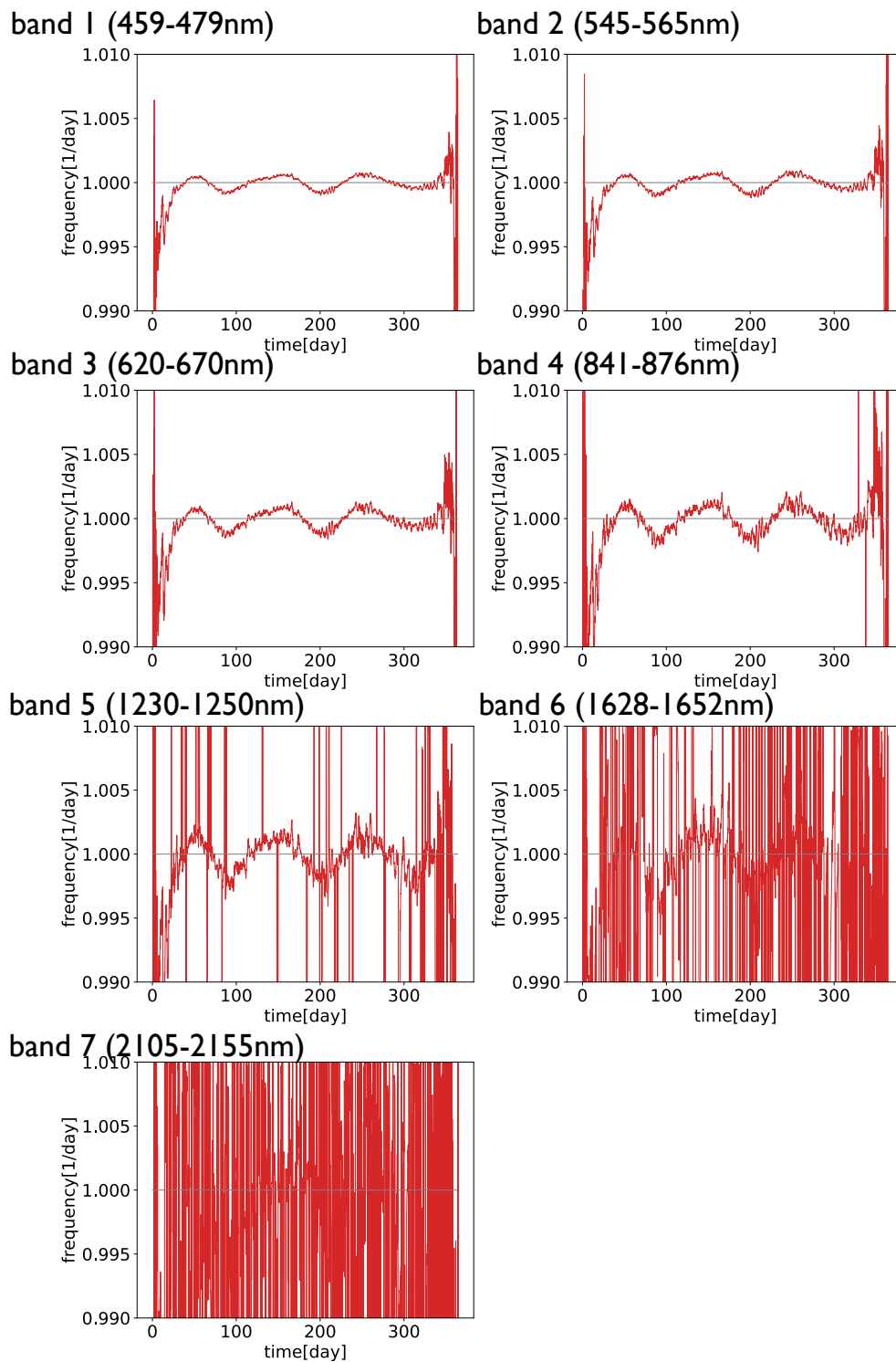


Figure 5.2: The estimated instantaneous frequency extracted from Figure 5.1 (bold red line) and the input frequency (thin gray line). Although the long-period (~ 100 days) modulation are seen in the upper panels, they follow the input frequency to some extent.

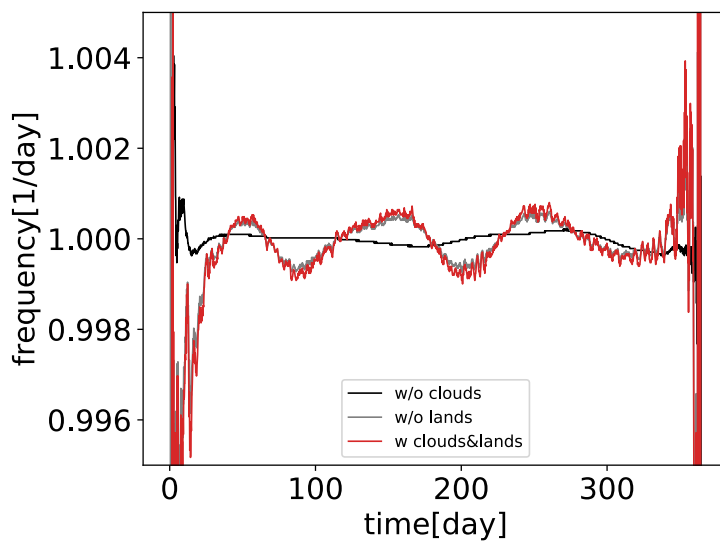


Figure 5.3: The extracted instantaneous frequencies of the band 1 light curves of the planet with lands and clouds (red), without lands (gray), and without clouds (black). Only the landless planet follows the fully planet.

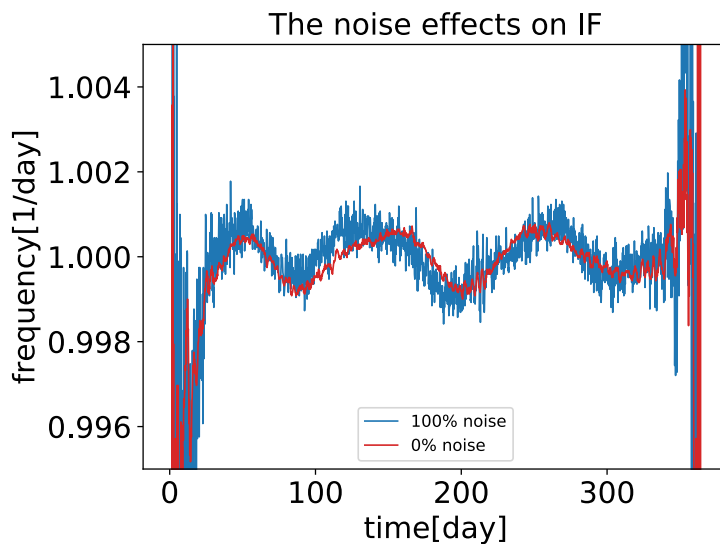


Figure 5.4: The extracted instantaneous frequencies for the light curves with no noise (red) and 100% noise (blue).

5.4 Obliquity dependence on the time-frequency representation

We aim to apply the frequency modulation method of the planetary obliquity estimation of Kawahara (2016) to the cloudy Earths with different obliquities. Before that, we see the obliquity dependence of the time-frequency representation of our simulated light curves.

At first we connect the data of 1 year periodically, not performing extensive mock observations, in order to obtain the fully clear light curves over a year. We perform the time-frequency representation of the planetary light curves by pseudo-Wigner distribution with the periodic boundary conditions as shown in Figure 5.5. We show the extracted instantaneous frequency curves (red lines) of the planet $\zeta = 0^\circ, 15^\circ, 30^\circ, 45^\circ, 60^\circ, 75^\circ,$ and 90° in Figure 5.6. The model curves obtained from the maximum weighted longitude approximation are shown by the gray lines. What we emphasize most in this figure is the instantaneous frequency curves of the three planets $\zeta = 0^\circ - 30^\circ$ follow the model curves very well. On the other hand those of highly oblique planets have less feature because of the fuzzy ridge of the time-frequency representation.

How do they occur the difference of the time-frequency representation? To check it, we first review our planetary light curves. Figure 5.8 shows the 1year planetary light curves of various obliquities with constant shifts. The vertical axis is based on the photon counts and we show the indication of their variability. Every light curves show about 100-150 photon counts per exposure time (3hours), about 2-3 times larger than those of cloudless Earth. Therefore, these variability of our simulated light curves are mainly caused by the inhomogeneity of clouds. We also see the seasonal variation of light curves: Highly oblique $\zeta \geq 30^\circ$ planets show the seasonal dip and thinning of diurnal variability during summer and the activation of diurnal variability during autumn for the North hemisphere. To approach the detail, we show the monthly light curves for each season in Figure 5.9. As the obliquity becomes larger, the amplitude of the diurnal variation becomes smaller and noisy. The variability activation on the highly oblique planets, shown in the light curve of the planet $\zeta = 90^\circ$ on July, does not show any obvious periodicity. The difference of the time-frequency representation exists before the time-frequency analysis. Next we should compare the results of light curves and GCM, such as the detailed dynamical motion of clouds. In section 3.3, we briefly showed the results of GCM. From small to middle oblique planets, the global cloud decreases were seen. It may correspond to the reduction of the amplitude of the diurnal periodicity. In cases of highly oblique planets, the clouds globally increase and reach the limit, in other words they become homogeneously cloudy and bright which makes non-periodical light curve variations. Figure 5.7 shows the planetary images of 0.0day. Highly oblique planets show the homogeneous brightness in their illuminated area while small oblique planets show some inhomogeneity. The non-periodical activation may imply the random thick cloud generation/extinction with a shorter lifetime than spin frequency. We have no climatological description of them

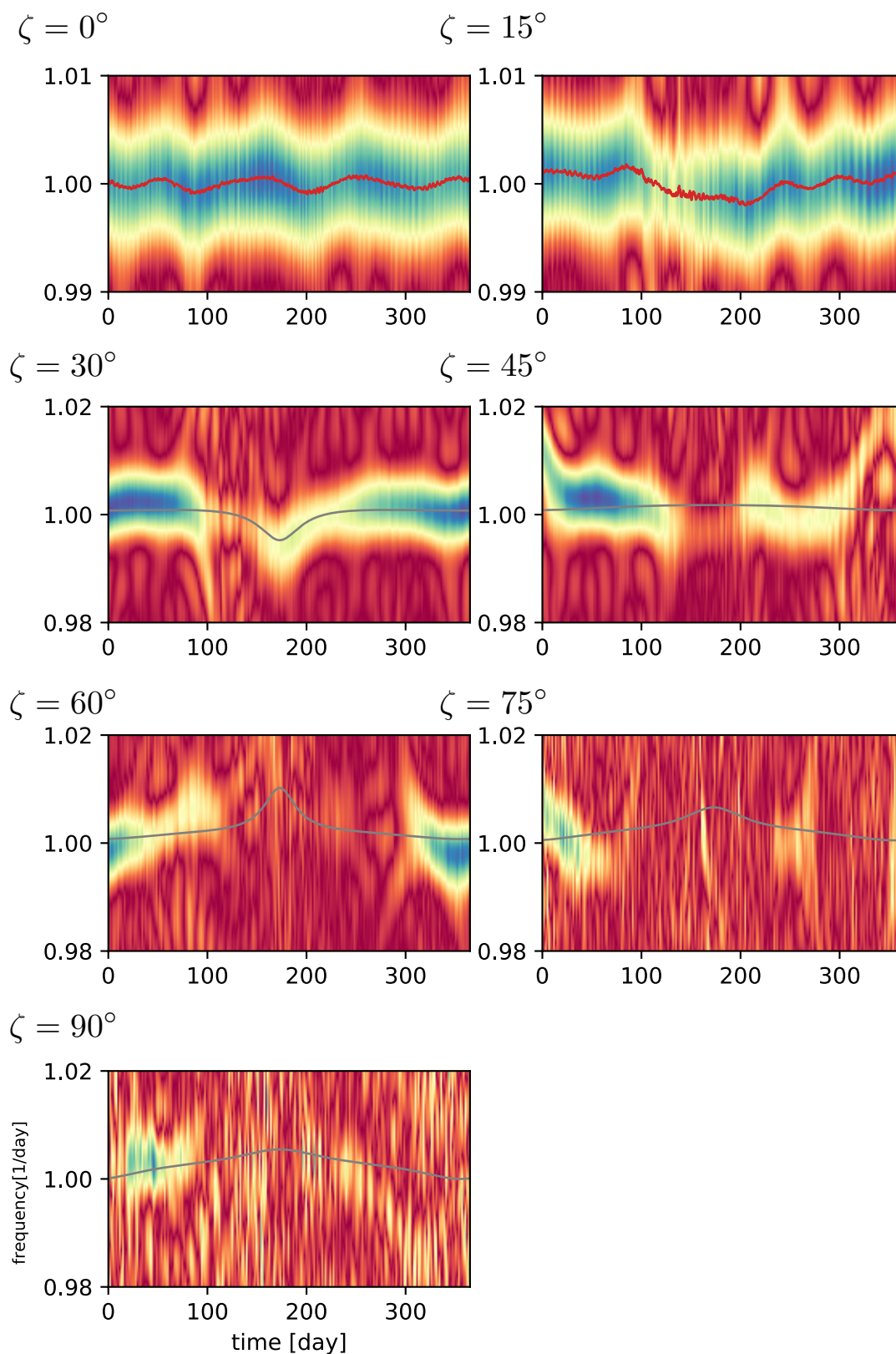


Figure 5.5: The time-frequency representations by pseudo-Wigner distribution for the light curves of planets with various obliquities ($\zeta = 0^\circ - 90^\circ$, every 15°). The red lines (in panels $\zeta = 0^\circ$ and 15°) show the extracted instantaneous frequency and the black lines show the model frequency predicted by Kawahara (2016).

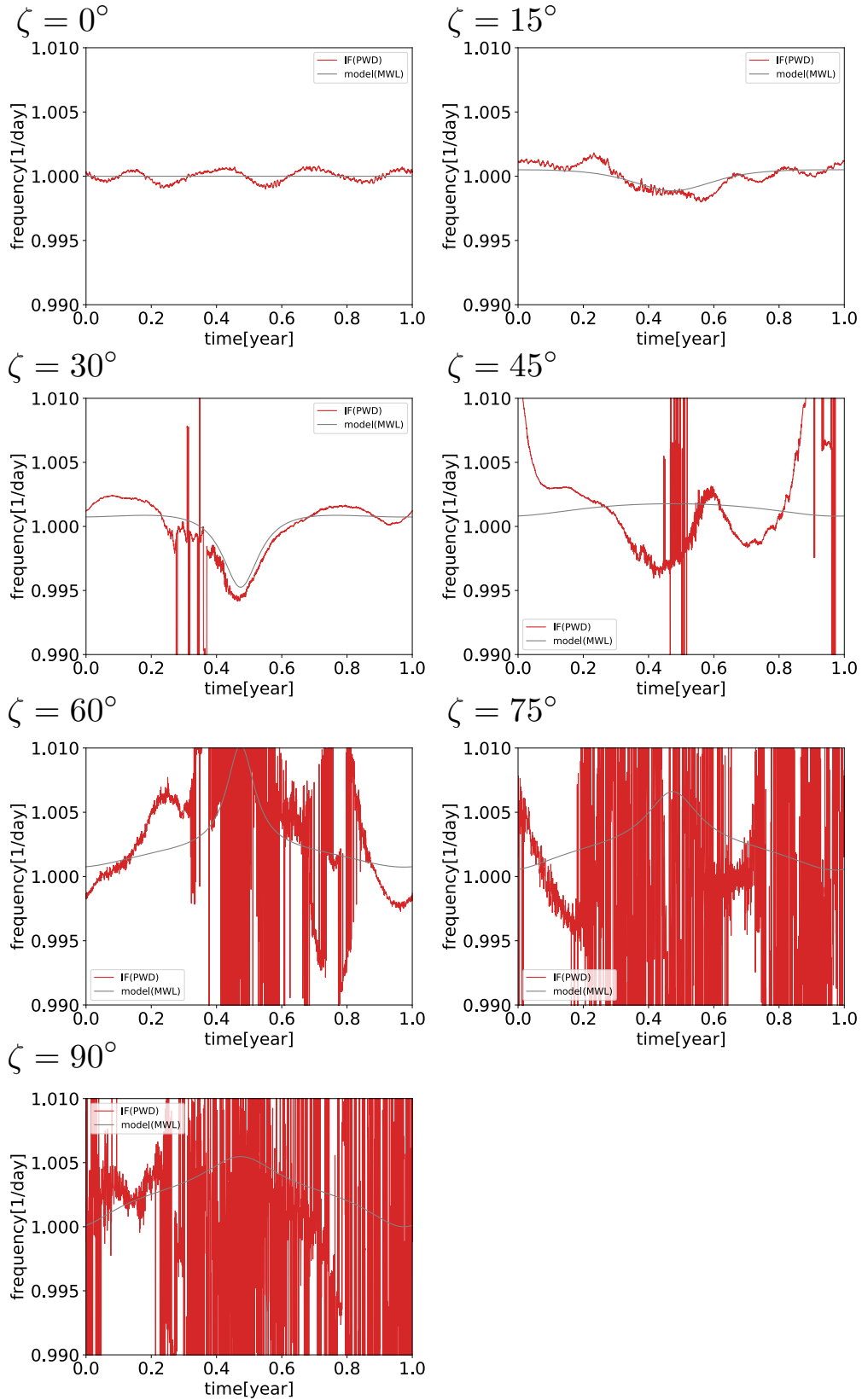


Figure 5.6: The extracted instantaneous frequencies for the light curves of planets with various obliquities ($\zeta = 0^\circ - 90^\circ$, every 15°). Those of small oblique planets ($\leq 30^\circ$) follow the model curves well.

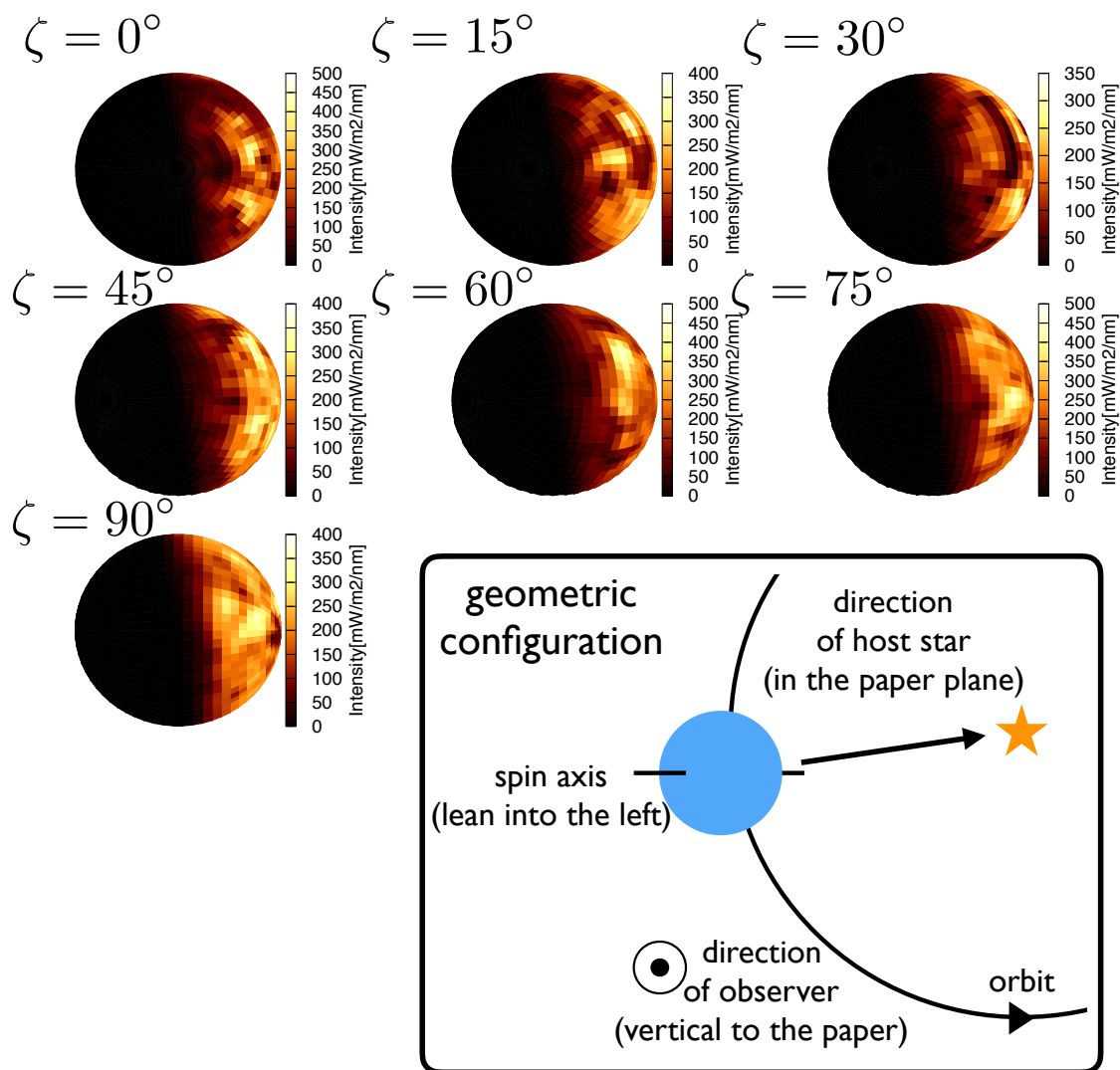


Figure 5.7: Images of planet with various obliquities ($\zeta = 0^\circ - 90^\circ$, every 15°). Highly oblique planets show the flat and bright images induced by its thick clouds.

for now. We extend the careful investigation on the results of light curves and GCM to the future study.

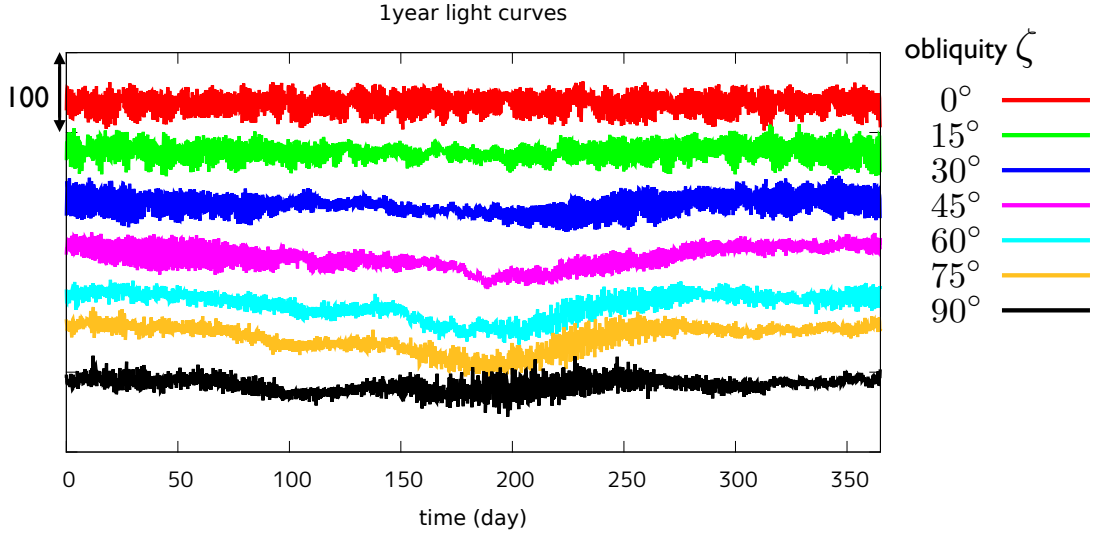


Figure 5.8: 1-year simulated light curves of the cloudy planets.

5.5 Estimation of the planetary obliquity

In this thesis, we use the two instantaneous frequency curves $\zeta = 0^\circ$ and 15° to estimate the obliquities of the input planet because they are showing the completely continuous modulation on their extracted instantaneous frequency. Although the planet of $\zeta = 30^\circ$ still shows the frequency modulation consistent with the model, we do not fit its frequency curve because some leaps are shown in the middle of the observation time. We postpone the obliquity estimation of highly (here, $\geq 30^\circ$) oblique planets. We also postpone the physical description of the obliquity dependence on the time-frequency representations.

Our fitting method is as follows. To find the best fit parameters, we use the Levenberg-Marquardt algorithm (mpfit, Markwardt 2009). This algorithm is a practical and fast algorithm of the least squares method for non-linear functions. We fix the two parameters $i = 0^\circ$ and $P_{\text{orb}} = 365.0[\text{day}]$. Basically the remaining free parameters are three; ζ , Θ_{eq} , and f_{spin} . In the case of $i = 0^\circ$, we cannot define the geometrical parameter Θ_{eq} because it degenerates. At the same time we cannot define the superior conjunction, which we use as the basis of the observation time. Therefore, we alternatively have to set another parameter determining the time basis, Θ_{offset} . Actually Θ_{offset} is equivalent to Θ_{eq} in the limit of $i \rightarrow 0$. We simply distinguish them. The input value of Θ_{offset} is 279.40° , corresponding to the orbital longitude from the vernal

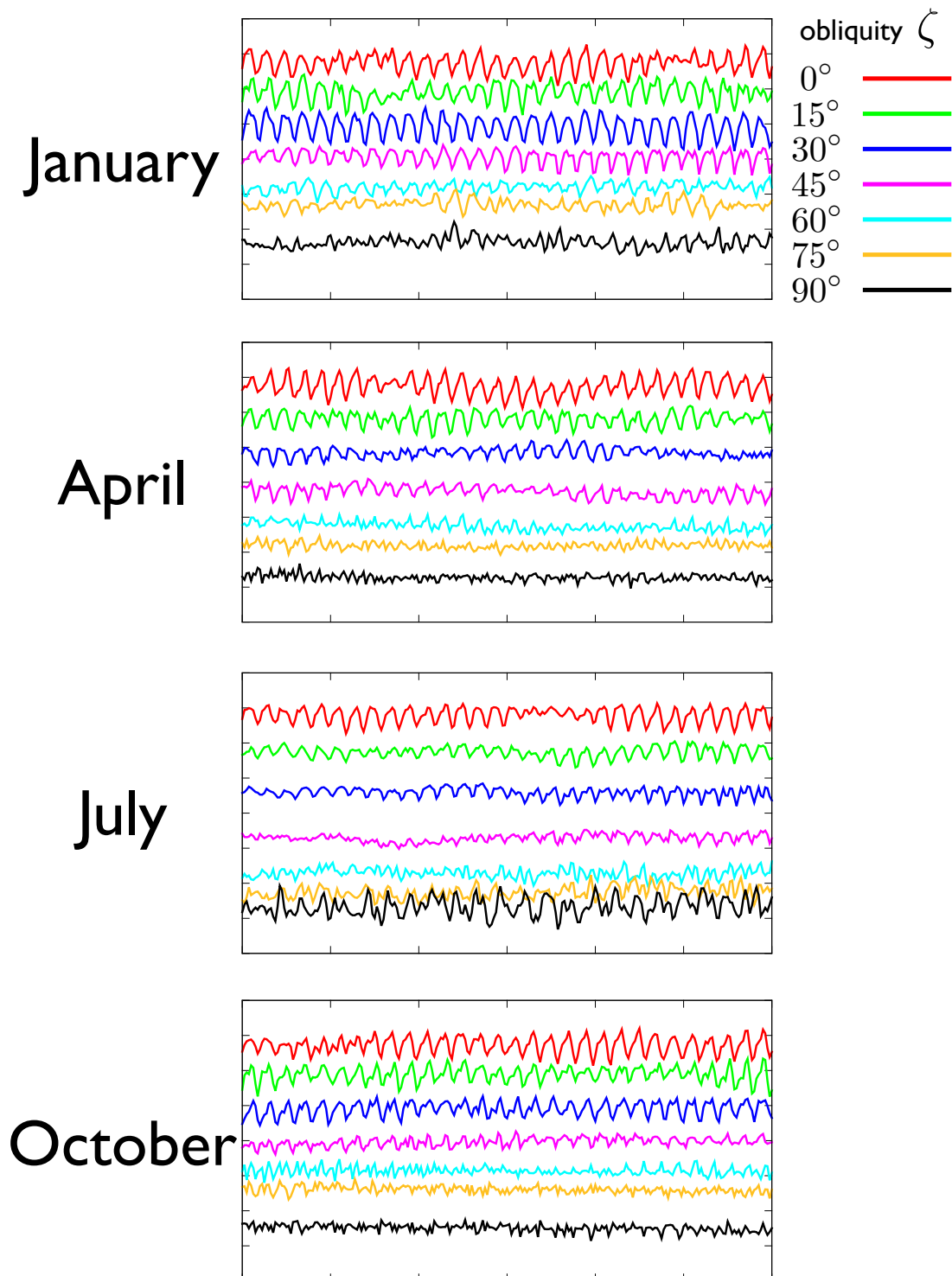


Figure 5.9: 1month simulated light curves of the cloudy planets.

equinox to the epoch of year (1/1, 0:00 GMT) of the Earth. We employ the sets of initial parameters as shown in Table 5.1. We find the parameter set which minimize the residual R defined to be

$$R = \sum_i (f(t_i) - f(\mathbf{d}, t_i))^2, \quad (5.1)$$

where $f(t_i)$ and $f(\mathbf{d}, t_i)$ are the extracted and model instantaneous frequency, and \mathbf{d} is a parameter set. To find the best fit, we run the fitting algorithm from several initial conditions as shown in 5.1. It also shows the fixed parameters we used.

Table 5.1: Initial and fixed parameter sets for best fit search

Initial parameter	value
obliquity ζ	$15i^\circ$ ($i = 1, 2, \dots, 12$)
Θ_{offset}	$60j^\circ$ ($j = 1, 2, \dots, 5$)
spin frequency f_{spin}	1.002740 [day ⁻¹]
Fixed parameter	value
orbital inclination i	0°
orbital frequency f_{orb}	0.002740 [day ⁻¹]

In the case of $\zeta = 0^\circ$, we find the two solutions. The two solutions correspond to the planet group with obliquity $\zeta = 0^\circ$ and 180° . The differences between the best-fit and input value are $\Delta\zeta \sim 2^\circ$ and $\Delta f_{\text{spin}} \sim 1\text{hr/yr}$. In principle, the frequency modulation method cannot distinct these two solutions because the modulation factor of both $\zeta = 0^\circ$ and 180° are flat.

In the case of $\zeta = 15^\circ$, We also find one solution which agrees well with the input value. The differences between the best-fit and input value are $\Delta\zeta \sim 4^\circ$, $\Delta\Theta_{\text{offset}} \sim 15^\circ$, and $\Delta f_{\text{spin}} \sim 1\text{hr/yr}$. We also show the residual map in the $(\Theta_{\text{offset}}, \zeta)$ projection in Figure 5.11.

Kawahara (2016) calculated the instantaneous frequency and estimated the planetary obliquity of the cloudless Earth. In this thesis, we do check the utility of the obliquity estimation of the Earth with clouds. In small oblique planets, we show that we can estimate the obliquity in spite of the dynamical effect of clouds with the estimation method using the frequency modulation proposed by Kawahara (2016). It indicates an interesting fact that the clouds trace the surface motion to some extent and they produce the light curve variability and frequency modulation similar to that of cloudless planets. The cloud subtracted Earth used in Kawahara (2016) indirectly requires to take the difference of the light curves between two photometric bands in order to suppress the effect of clouds, but our estimation successfully, limited to the small oblique planets, retrieve the planetary obliquity. We do not use the extracted instantaneous frequencies of highly oblique planets because we have not confirmed their results of climate. We postpone them to a future work.

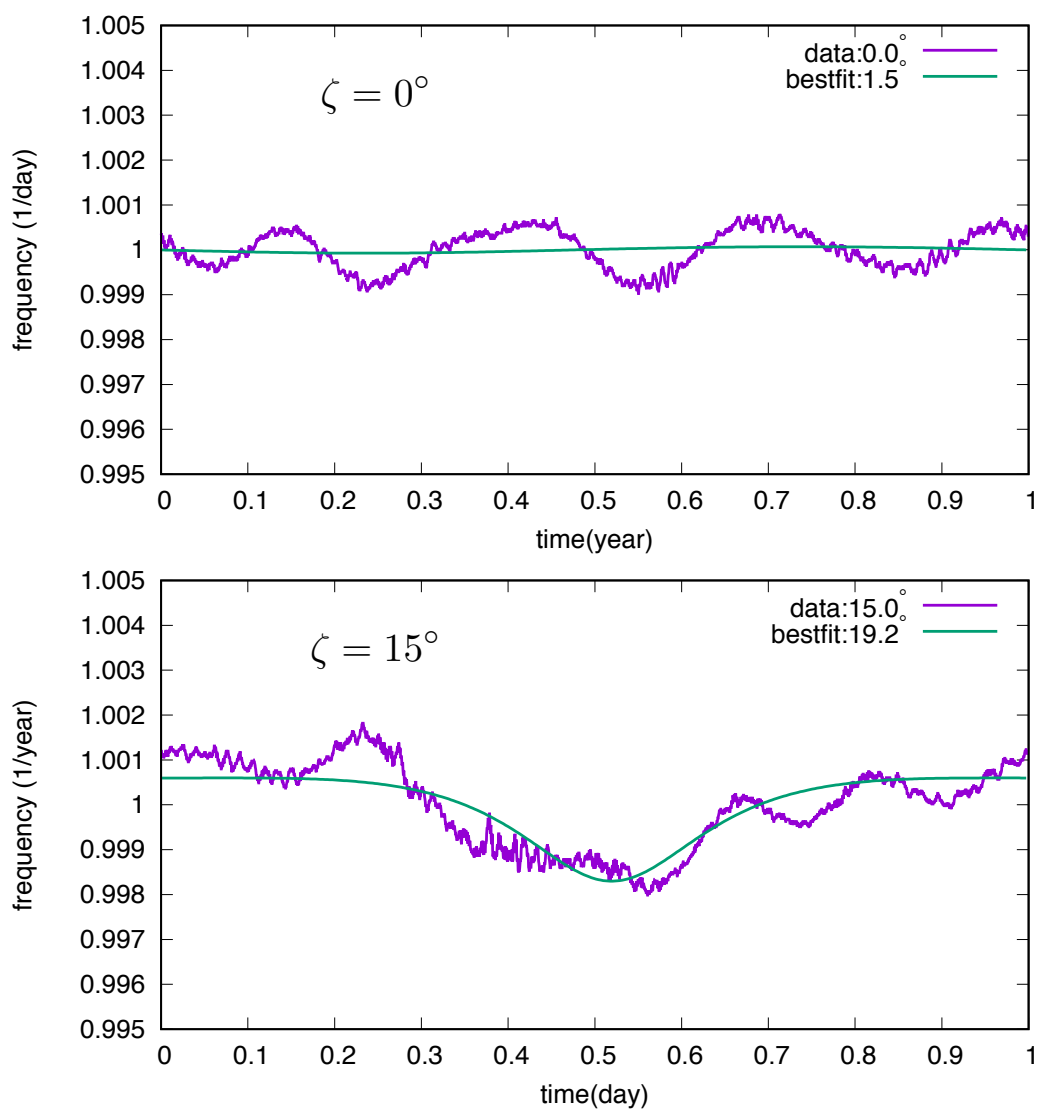


Figure 5.10: Comparison of frequency curves. Upper and lower panel show the fitting results of the input obliquity $\zeta = 0^\circ$ and 15° . We plot the extracted instantaneous frequency curve and the model curves.

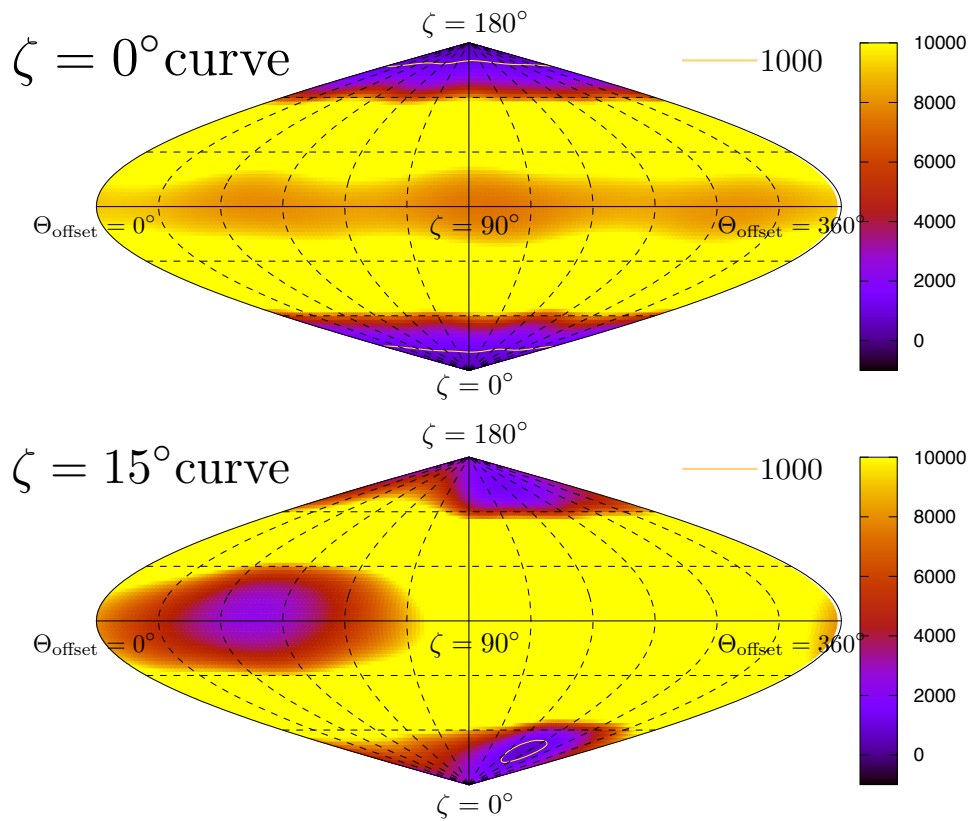


Figure 5.11: R map in the $(\Theta_{\text{offset}}, \zeta)$ plane. The best-fit region is closed by the yellow line, corresponding to the input value. In the case of $\zeta = 0^\circ$, where in principle we cannot distinguish from the completely retrograde $\zeta = 180^\circ$ planet, the R map shows the two solutions around $\zeta = 0^\circ$ and 180° .

Chapter 6

Summary and Future prospects

Time resolved direct imaging of exoplanets and its light curve analysis for the characterization of the environments of exoplanets has been intensively studied. The previous study suggesting a promising analysis method to detect the planetary obliquity, Kawahara (2016), gave a simple model of the frequency modulation of diurnal variability induced by the spin and orbital motion. However, their simulation were based on the assumption of cloudless Earth.

In this thesis, we studied the cases of cloudy Earths by using a public GCM, DC-PAM5 (Takahashi et al. 2016), for the consistent expression of the dynamical motion of clouds. We also utilized a public radiative transfer code, libRadtran-2.0.1 (Mayer & Kylling 2005), for the mock observation of cloudy Earths and the time-frequency analysis code for the extraction of frequency modulation (juwvid, Kawahara 2016).

In the little obliquity cases $\zeta = 0^\circ$ and 15° , we gave good estimations of the planetary obliquity and spin frequency, with the difference between the input and best-fit value of $\Delta\zeta \sim 4^\circ$, $\Delta\Theta_{\text{offset}} \sim 15^\circ$, and $\Delta f_{\text{spin}} \sim 1\text{hr/yr}$. We found another best-fit parameters of $\zeta \sim 180^\circ$ from $\zeta = 0^\circ$ frequency modulation fitting, which in principle could not be distinguished them. Note that our estimation method uses the single band directly, without removing the effect of clouds, while the cloud-subtracted Earth model used in Kawahara (2016) was secondarily using the color difference of multi band light curves to remove the effect of clouds. It indicates that the clouds of small oblique planets almost follow the spin motion, in other words the relative motion to the surface is small and the lifetime of clouds are longer than the spin frequency.

We could not extract the obvious frequency modulation of highly oblique planets, while we could easily extract the clear frequency modulation from the light curves of small oblique planets enough to estimate the planetary obliquity. We extend the obliquity estimation of highly oblique planets. These obliquity dependence was also seen in the light curves themselves. Small oblique planets showed the clear 1day periodicity with large amplitudes. Middle oblique planets have a small and non-periodic variation term because the clouds become globally thin. Highly oblique planets have the non-periodic variation over a year preventing us from extracting the diurnal periodicity. Because we have never prepared climatological descriptions on these light curves, we extend the further discussion.

Acknowledgments

I would like to express my gratitude to my supervisor, Prof. Yasushi Suto, who encouraged me to advance my research. Without his precise advices and help, I could not have finished this thesis. I am also grateful to Dr. Takanori Kodama, Prof. Masaki Ishiwatari, and Prof. Hajime Kawahara, who gave me insights into climatology and exoplanet science. I have learned their attitude to science and the way of simulating models and analyzing data. I thank to Kento Masuda, Shoya Kamiaka, Masataka Aizawa, and Kou Hosokawa for attending my seminar and giving me suggestive comments. I also thank to the members of the UTAP (Theoretical Astrophysics group) for providing me comfortable and cheerful environments. I would like to express my gratitude to my previous colleagues in Kyoto University for encouraging me in my studies in University of Tokyo.

Finally, I would like to thank my family, who continue to support my life.

Bibliography

- Abe, Y., Numaguti, A., Komatsu, G., & Kobayashi, Y. 2005, *Icarus*, 178, 27
- Anderson, G. P. 1986, AFGL atmospheric constituent profiles (0-120km)
- Anglada-Escudé, G., Amado, P. J., Barnes, J., et al. 2016, *Nature*, 536, 437
- Arakawa, A., & Suarez, M. J. 1983, *Monthly Weather Review*, 111, 34
- Beljaars, A. C. M., & Holtslag, A. A. M. 1991, *Journal of Applied Meteorology*, 30, 327
- Beljaars, A. C. M., & Viterbo, P. 1994, *Boundary-Layer Meteorology*, 71, 135
- Berta, Z. K., Charbonneau, D., Désert, J.-M., et al. 2012, *ApJ*, 747, 35
- Cowan, N. B., Agol, E., Meadows, V. S., et al. 2009, *ApJ*, 700, 915
- Emde, C., Buras-Schnell, R., Kylling, A., et al. 2016, *Geoscientific Model Development*, 9, 1647
- Ford, E. B., Seager, S., & Turner, E. L. 2001, *Nature*, 412, 885
- Fujii, Y., & Kawahara, H. 2012, *ApJ*, 755, 101
- Fujii, Y., Kawahara, H., Suto, Y., et al. 2011, *ApJ*, 738, 184
- . 2010, *ApJ*, 715, 866
- Greengard, L., & Lee, J.-Y. 2004, *SIAM Review*, 46, 443
- Henry, G. W., Marcy, G. W., Butler, R. P., & Vogt, S. S. 2000, *ApJ*, 529, L41
- Hu, Y. X., & Stamnes, K. 1993, *Journal of Climate*, 6, 728
- Ishiwatari, M., Nakajima, K., Takehiro, S., & Hayashi, Y.-Y. 2007, *Journal of Geophysical Research (Atmospheres)*, 112, D13120
- Ishiwatari, M., Takehiro, S.-I., Nakajima, K., & Hayashi, Y.-Y. 2002, *Journal of Atmospheric Sciences*, 59, 3223

- Kawahara, H. 2016, *ApJ*, 822, 112
- Kawahara, H., & Fujii, Y. 2011, *ApJ*, 739, L62
- Kuzuhara, M., Tamura, M., Kudo, T., et al. 2013, *ApJ*, 774, 11
- Le Trent, H., & Li, Z.-X. 1991, *Climate Dynamics*, 5, 175
- Manabe, S. 1969, *Monthly Weather Review*, 97, 739
- Markwardt, C. B. 2009, in *Astronomical Society of the Pacific Conference Series*, Vol. 411, *Astronomical Data Analysis Software and Systems XVIII*, ed. D. A. Bohlender, D. Durand, & P. Dowler, 251
- Marois, C., Macintosh, B., Barman, T., et al. 2008, *Science*, 322, 1348
- Mayer, B., & Kylling, A. 2005, *Atmospheric Chemistry and Physics*, 5, 1855
- Mayor, M., & Queloz, D. 1995, *Nature*, 378, 355
- Mellor, G. L., & Yamada, T. 1982, *Reviews of Geophysics and Space Physics*, 20, 851
- Moorthi, S., & Suarez, M. J. 1992, *Monthly Weather Review*, 120, 978
- Nakajima, T. 1983, *J. Quant. Spec. Radiat. Transf.*, 29, 521
- Noda, S., Ishiwatari, M., Nakajima, K., et al. 2017, *Icarus*, 282, 1
- Rossow, W. B. 1978, *Icarus*, 36, 1
- Salomonson, V. V., Barnes, W. L., Maymon, P. W., Montgomery, H. E., & Ostrow, H. 1989, *IEEE Transactions on Geoscience and Remote Sensing*, 27, 145
- Seager, S. 2010, *Exoplanets*
- Stamnes, K., Tsay, S.-C., Jayaweera, K., & Wiscombe, W. 1988, *Appl. Opt.*, 27, 2502
- Takahashi, Y. O., Fujiwara, H., Fukunishi, H., et al. 2003, *Journal of Geophysical Research (Planets)*, 108, 5018
- Takahashi, Y. O., Kashimura, H., Takehiro, S., et al. 2016, <http://www.gfd-dennou.org/library/dcpam/>
- Turbet, M., Forget, F., Leconte, J., Selsis, F., & Bolmont, E. 2017, *LPI Contributions*, 2042, 4016
- Wanner, W., Li, X., & Strahler, A. H. 1995, *Journal of Geophysical Research: Atmospheres*, 100, 21077
- Williams, D. M., & Pollard, D. 2003, *International Journal of Astrobiology*, 2, 1